

Role of Mesoscale Eddies in Cross-Frontal Transport of Heat and Biogeochemical Tracers in the Southern Ocean

CAROLINA O. DUFOUR,^{*} STEPHEN M. GRIFFIES,⁺ GREGORY F. DE SOUZA,^{*,&} IVY FRENGER,^{*}
ADELE K. MORRISON,^{*} JAIME B. PALTER,^{#,**} JORGE L. SARMIENTO,^{*} ERIC D. GALBRAITH,[@]
JOHN P. DUNNE,⁺ WHIT G. ANDERSON,⁺ AND RICHARD D. SLATER^{*}

^{*} *Atmospheric and Oceanic Sciences Program, Princeton University, Princeton, New Jersey*

⁺ *NOAA/Geophysical Fluid Dynamics Laboratory, Princeton, New Jersey*

[#] *Department of Atmospheric and Oceanic Science, McGill University, Montreal, Quebec, Canada*

[@] *Department of Earth and Planetary Science, McGill University, Montreal, Quebec, Canada*

(Manuscript received 26 November 2014, in final form 24 August 2015)


ABSTRACT

This study examines the role of processes transporting tracers across the Polar Front (PF) in the depth interval between the surface and major topographic sills, which this study refers to as the “PF core.” A preindustrial control simulation of an eddying climate model coupled to a biogeochemical model [GFDL Climate Model, version 2.6 (CM2.6)–simplified version of the Biogeochemistry with Light Iron Nutrients and Gas (miniBLING) 0.1° ocean model] is used to investigate the transport of heat, carbon, oxygen, and phosphate across the PF core, with a particular focus on the role of mesoscale eddies. The authors find that the total transport across the PF core results from a ubiquitous Ekman transport that drives the upwelled tracers to the north and a localized opposing eddy transport that induces tracer leakages to the south at major topographic obstacles. In the Ekman layer, the southward eddy transport only partially compensates the northward Ekman transport, while below the Ekman layer, the southward eddy transport dominates the total transport but remains much smaller in magnitude than the near-surface northward transport. Most of the southward branch of the total transport is achieved below the PF core, mainly through geostrophic currents. This study finds that the eddy-diffusive transport reinforces the southward eddy-advective transport for carbon and heat, and opposes it for oxygen and phosphate. Eddy-advective transport is likely to be the leading-order component of eddy-induced transport for all four tracers. However, eddy-diffusive transport may provide a significant contribution to the southward eddy heat transport due to strong along-isopycnal temperature gradients.

1. Introduction

The Southern Ocean (south of 30°S) is a key region for the meridional transport of heat and biogeochemical tracers and one of the few places in the global ocean where ancient deep waters are exposed to the atmosphere

(Marshall and Speer 2012; Talley 2013; Morrison et al. 2015). Within the latitudes of the Antarctic Circumpolar Current (ACC), vigorous wind-driven upwelling brings old waters, poor in oxygen and rich in natural carbon and nutrients, to the surface. Once upwelled, much of the water heads northward in the surface layer, driven by an intense Ekman transport. At the northern boundary of the ACC, it reaches the formation sites of Antarctic Intermediate Water (AAIW) and Subantarctic Mode Water (SAMW). AAIW and SAMW are then subducted into the ocean interior together with heat, carbon, oxygen, and nutrients. Upwelling and subduction are thus important mechanisms for ventilation of the deep ocean (DeVries and Primeau 2011; Khatiwala et al. 2012) and for long-term sequestration of physical and biogeochemical anomalies, as well as for the export of nutrients to low latitudes (Sarmiento et al. 2004; Palter et al. 2010).

 Denotes Open Access content.

[&] Current affiliation: ETH Zurich, Institute of Geochemistry and Petrology, Zurich, Switzerland.

^{**} Current affiliation: Graduate School of Oceanography, University of Rhode Island, Narragansett, Rhode Island.

Corresponding author address: Carolina O. Dufour, Program in Atmospheric and Oceanic Sciences, 300 Forrester Road, Sayre Hall, Princeton, NJ 08544.
E-mail: cdufour@princeton.edu

DOI: 10.1175/JPO-D-14-0240.1

© 2015 American Meteorological Society

However, meridional transport in the Southern Ocean requires crossing multiple intense jets that form the ACC fronts and act as natural barriers to tracer transport. Both observational and experimental studies have demonstrated that mixing across the core of jets is strongly inhibited due to the speed of the jet being higher than the propagation speed of eddies, hence reducing the time during which eddies can stir tracers (e.g., Bower et al. 1985; Lozier et al. 1997; Sommeria et al. 1989; Ferrari and Nikurashin 2010). Nonetheless, strong perturbations, such as rings detaching from the front, might provide a way for tracers to cross the jet cores (Samelson 1992; Wiggins 2005). Enhanced cross-frontal transport occurs primarily in two regions of the jets: in the Ekman layer and at the critical levels (also called steering levels). In the Ekman layer (the upper ~100–200 m), studies have reported vigorous cross-frontal transport driven by northward Ekman flow (Rintoul and England 2002; Ito et al. 2010; Palter et al. 2013; Holte et al. 2013). At critical levels, observations, theory, and models have diagnosed high effective eddy diffusivities, attributed to the rate at which mesoscale eddies stir properties on interior isopycnal surfaces (Smith and Marshall 2009; Abernathey et al. 2010; Naveira Garabato et al. 2011). These critical levels follow the outer boundary of the jet core, from the edges of the jet to the deepest extension of its core, which typically lies between 1 and 1.5 km, and correspond to the depths where eddies drift at the same speed as the jet. Hence, mesoscale eddies might well be another important driver of the cross-frontal tracer transport.

Mesoscale eddies are known to transport tracers through two processes: Eddy-advective transport [also known as the Gent and McWilliams (1990) effect] results from the eddies extracting the potential energy imparted by winds from the mean flow, inducing a flattening of isopycnal surfaces, and hence opposing the wind-driven circulation (i.e., Ekman and geostrophic transport; Gent and McWilliams 1990; Gent et al. 1995). Eddy-diffusive transport (also known as isopycnal or neutral diffusion) results from the eddies stirring tracers along interior isopycnal surfaces, inducing a downgradient tracer flux (Solomon 1971; Redi 1982). Eddy-advective and eddy-diffusive transports can either reinforce or oppose each other, and their relative importance varies as a function of the time-scale considered and the distribution and mixed layer residence time of the biogeochemical tracer they act upon (Lee et al. 1997).

As a region of strong baroclinic instability, the Southern Ocean spawns a rich mesoscale eddy field. Where the ACC is unbounded, that is generally above ~2 km, there are no net along-stream pressure gradients

to support cross-stream geostrophic currents. Hence, cross-frontal tracer transport should mainly result from the competition between Ekman transport and eddy transport (advective and diffusive contributions), with eddies as the main conveyer of tracer transport below the Ekman layer. Marshall and Speer (2012) thus argue that mesoscale eddies play a leading role in driving the upwelling of deep waters to the Antarctic Divergence (~60°S). Additionally, enhanced eddy activity has been reported in specific locations along the path of the ACC, inducing intense cross-frontal transport (e.g., Naveira Garabato et al. 2011; Thompson and Sallée 2012). Where the fronts flow around major topographic obstacles, hence developing large-scale meanders, departures from parallel flow conditions break the prevalent regime where cross-frontal transport is inhibited (Naveira Garabato et al. 2011). Such “hotspots” of transport, or “leaky jet” segments, show enhanced effective eddy diffusivity, thus allowing more tracer transport across the fronts (Naveira Garabato et al. 2011; Thompson and Sallée 2012; Sallée et al. 2008b).

Despite its importance, the net effect of the mesoscale eddy activity on the cross-frontal transport of climate relevant tracers such as heat, carbon, oxygen, and nutrients has not yet been elucidated. The investigation of processes driving the cross-frontal transport of tracers, in particular mesoscale eddies, remains a challenge due to the scarcity of observations. On the modeling side, however, this investigation has recently become feasible due to the advent of eddying climate models coupled to biogeochemical components.

In this study, we address the role of mesoscale eddies in the transport of heat and biogeochemical tracers across the fronts of the ACC. We focus on regions where (i) jets are strong, hence providing a barrier to tracer transport, and (ii) mean cross-stream geostrophic transport cannot take place, so that eddies are the dominant driver of tracer transport below the Ekman layer. In these regions, referred to as the core of the fronts, our goal is twofold: 1) to quantify the net contribution of the mesoscale eddy field to cross-frontal tracer transport and 2) to disentangle the respective roles of eddy-advective and eddy-diffusive components on cross-frontal tracer transport.

To achieve our goals, we make use of an eddy-rich ocean–atmosphere climate model coupled to a simplified ocean biogeochemical model [GFDL Climate Model, version 2.6 (CM2.6)–simplified version of Biogeochemistry with Light Iron Nutrients and Gas (miniBLING) model] in order to investigate the role of resolved mesoscale eddies in transporting tracers across the core of fronts. We focus on the Polar Front (PF), one of the main fronts of the ACC and the northern boundary

of the Antarctic Divergence, which is where most deep waters upwell. The investigation is carried out in a preindustrial simulation to avoid the complexity induced by transient forcing, in particular for heat and carbon. Advection budget terms computed online in the model allow us to accurately calculate the transport across the PF core and decompose the transport into time-mean and eddy components. Details of the model and methods are provided in [section 2](#). Results are presented with an emphasis on heat and carbon in [section 3a](#). In [section 3b](#), we highlight differences between tracers arising from the along-isopycnal tracer gradients. In [section 4](#), we discuss limitations of our approach. We also compare results for another front, the Subantarctic Front (SAF), to that of the PF. We close the paper in [section 5](#) with a summary of the main results. Finally, we offer two appendices that expand on the method.

2. Methods

a. Model and simulation

We briefly present here some aspects of the physical and biogeochemical components of the climate model used in this study that are of relevance to the cross-frontal transport of tracers in the Southern Ocean. For further details, the reader is referred to [Delworth et al. \(2012\)](#) and [Griffies et al. \(2015\)](#) for a description of the physical component (CM2.6) and to [Galbraith et al. \(2015, manuscript submitted to *J. Adv. Model. Earth Syst.*\)](#) for a description of the biogeochemical ocean component (miniBLING).

1) CM2.6–MINIBLING

CM2.6 is a coupled climate model first introduced by [Delworth et al. \(2012\)](#) and further analyzed by [Griffies et al. \(2015\)](#). The model uses an atmospheric component of roughly 50-km horizontal resolution as well as sea ice and land model components. The oceanic component is based on the Modular Ocean Model, version 5 (MOM5; [Griffies 2012](#)) run with volume-conserving Boussinesq kinematics and a z^* vertical coordinate. The vertical resolution is 50 levels with a thickness of 10 m at the surface increasing with depth to 210 m. The horizontal grid spacing is 0.1° , corresponding to a grid size of 5.5 km at 60°S . The horizontal resolution is thus fine enough to simulate a rich mesoscale eddy field in the Southern Ocean, as shown in [Delworth et al. \(2012\)](#) and [Griffies et al. \(2015\)](#). However, we note that the mesoscale eddy spectrum is not fully resolved, in particular near the coasts and south of 60°S ([Hallberg 2013](#)). CM2.6 is run with no lateral tracer diffusion. The submesoscale mixed

layer eddy parameterization of [Fox-Kemper et al. \(2011\)](#) is applied to account for the restratification effect of submesoscale eddies in the mixed layer that the 0.1° horizontal grid spacing is not able to resolve. However, no mesoscale eddy transport parameterization is used in the tracer equation, so that our study focuses only on mesoscale processes that are explicitly resolved in the model.

Because of the computational cost of adding tracers to a 0.1° coupled climate model, a simplified version of the prognostic biogeochemical model Biogeochemistry with Light Iron Nutrients and Gas (BLING) ([Galbraith et al. 2010](#)), called miniBLING, has been developed. While the core ecosystem behavior of miniBLING remains identical to BLING, the number of prognostic tracers has been reduced to three, namely, dissolved inorganic carbon (DIC), a dissolved inorganic macronutrient (called PO_4), and dissolved oxygen (O_2). The macronutrient PO_4 is intended to represent the limiting macronutrient, which is generally NO_3 in the real ocean. Here, it is called PO_4 to be clear that it does not include N_2 fixation or denitrification. The reduction of tracers has been accomplished by eliminating dissolved organic phosphate via an altered representation of PO_4 recycling, with more rapid near-surface recycling of PO_4 under low PO_4 conditions. The BLING prognostic iron tracer has been replaced with a prescribed monthly iron climatology computed from a 1° simulation using BLING. The carbonate equilibria at the ocean's surface are dependent on prognostic temperature, salinity, and DIC, with surface alkalinity prescribed at each time step as a function of model salinity, using a 2D alkalinity–salinity linear regression based on observed global maps ([Garcia et al. 2010a](#); [Key et al. 2004](#)). MiniBLING uses parameter values chosen for BLING based on a 3° global ocean-only simulation, which were not “tuned” for the 0.1° ocean of CM2.6. A detailed description and evaluation of the miniBLING model can be found in [Galbraith et al. \(2015, manuscript submitted to *J. Adv. Model. Earth Syst.*\)](#).

2) PREINDUSTRIAL SIMULATION

A simulation of the CM2.6–miniBLING model is run with the atmospheric CO_2 concentration fixed at 286 ppm corresponding to the preindustrial level of the year 1860. The ocean is started from rest with temperature and salinity fields initialized to *World Ocean Atlas 2009* (WOA; [Garcia et al. 2010a](#); [Locarnini et al. 2010](#)). PO_4 and O_2 fields are initialized to WOA ([Garcia et al. 2010a,b](#)), and DIC fields are initialized to the Global Ocean Data Analysis Project (GLODAP) corrected for preindustrial values ([Key et al. 2004](#)). MiniBLING is included starting at year 48, thus allowing for the

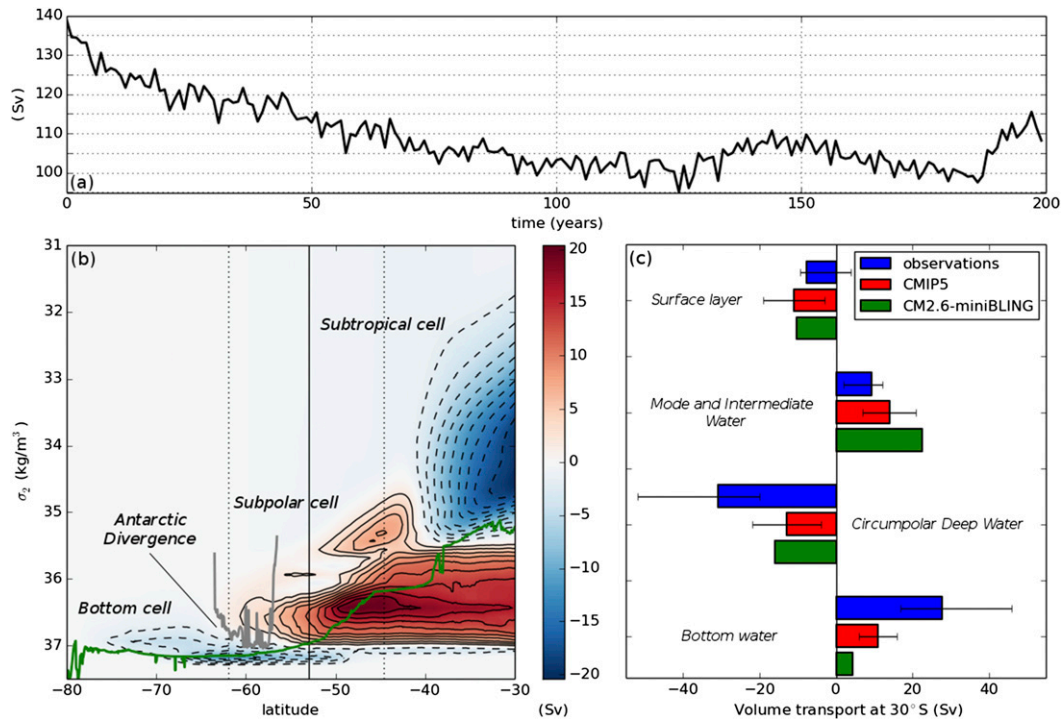


FIG. 1. (a) Time series of the transport at Drake Passage in the CM2.6–miniBLING simulation. (b) Meridional overturning circulation in σ_2 coordinates averaged over the last 20 yr of the CM2.6–miniBLING simulation, with σ_2 the potential density referenced at 2000 m. Red cells indicate clockwise flow while blue cells indicate counterclockwise flow with a 2-Sv contour interval. The solid vertical line indicates the mean latitude of the PF with the dashed lines showing the range of latitudes that the PF occupies. The green line indicates the density of the zonal maximum of the September mixed layer depth and the gray line indicates the topographic sill depth at the latitudes of Drake Passage. Note that the mixed layer is very deep south of $\sim 60^\circ$ S due to the occurrence of a polynya in the Weddell Sea. (c) Transport summed into different water mass classes from (blue) observation-based estimates, (red) the phase 5 of the Coupled Model Intercomparison Project (CMIP5) multimodel ensemble mean, and (green) the CM2.6–miniBLING simulation. Transports are estimated in a latitude range of 30° to 40° S in observations and are computed at 30° S in models. Error bars show the minimum and maximum of the observation-based datasets (on top of blue bars) and the CMIP5 multimodel standard deviation (on top of red bars) for each water mass class. The compilation of estimates from observations and the CMIP5 model ensemble, and the method used to find water mass boundaries, are described in Sallée et al. (2013). A similar method was applied to the last 20 yr of CM2.6–miniBLING output.

physical circulation to partially adjust. The simulation is run for 200 yr in total, that is, 152 yr for biogeochemistry. In this study, the last 20 yr of the simulation (years 181 to 200) are investigated.

3) EVALUATION OF CM2.6–MINIBLING

Here, we briefly compare the simulated physical transport and tracer distributions with observations.

The simulated transport across Drake Passage stabilizes at around 100 Sverdrups (Sv; $1 \text{ Sv} = 10^6 \text{ m}^3 \text{ s}^{-1}$) after ~ 120 yr of downward drift (Fig. 1a). This value is lower than the observational estimates ranging from 110 to 170 Sv (e.g., Whitworth 1983; Whitworth and Peterson 1985; Cunningham et al. 2003; Chidichimo et al. 2014). The weak ACC transport is most likely related to a lack of formation and overflow of dense waters formed along

the Antarctic coasts that are not properly represented in the CM2.6 simulation (see Fig. 1c). A comparison of meridional sections between the model and WOA (not shown) reveals that the density structure of the model collapses at depth south of the ACC due to a lack of overflow of dense waters formed on the Antarctic shelves. Inhibited overflows are typical of z -coordinate models, as noted by Winton et al. (1998) and Legg et al. (2006). However, within the top 1.5 km of the ACC, the density structure of the model is similar to the observations, so that the jet intensity is not affected by the weak ACC. In addition, the occurrence of two Weddell Sea polynya events in the simulation, one starting in year 127 and the other in year 184 and both lasting ~ 20 yr, leads to intense deep convection that temporarily boosts the ACC transport by ~ 10 Sv through an

increase in the meridional pressure gradient, as reported in previous modeling studies (Hirabara et al. 2012; Shakespeare and Hogg 2012; Cheon et al. 2014; Spence et al. 2014).

The meridional overturning circulation (MOC) averaged over the last 20 yr of the simulation shows a maximum of ~ 20 Sv in the subtropical cell, ~ 20 Sv in the subpolar cell, and ~ 10 Sv in the bottom cell (Fig. 1b). These cells correspond respectively to light subtropical waters flowing to the south and being transformed into SAMW as they cool (subtropical cell); upper circumpolar deep waters (UCDW) flowing southward and upward and being transformed into AAIW and SAMW by surface fluxes (subpolar cell); and lower circumpolar deep waters (LCDW) flowing farther south, transforming into dense waters through heat loss and brine rejection near the Antarctic coasts, and then sinking before becoming Antarctic Bottom Waters (AABW) (bottom cell). These transports lie well within the broad range of model estimates (subtropical cell: -11 to 30 Sv; subpolar cell: 8 to 18 Sv; bottom cell: -3 to -20 Sv; e.g., Hallberg and Gnanadesikan 2006; Ballarotta et al. 2013; Dufour et al. 2012). However, there is less agreement with observation-based estimates, as the main return path for circumpolar deep waters in the model is through the formation of AAIW, whereas observational estimates suggest more transforms into AABW (Fig. 1c). This is a feature shared by many models, as highlighted in previous studies (Downes et al. 2011; Sallée et al. 2013).

The simulation is initialized with observational climatologies [see section 2a(2)] that provide a reference to evaluate how the model drifts from its initial state. Figure 2 shows a comparison between these observational climatologies and the last 20 yr of the simulation for surface temperature, salinity, DIC, PO_4 , and O_2 . While the large-scale patterns and values of the simulated variables are overall in good agreement with observations, some discrepancies exist. The simulation is generally cooler than observations at the surface, an expected difference as the simulation does not experience the climate warming of the industrial era. The simulation is also generally fresher than observations at the surface. A strong warm and saline anomaly with respect to observations shows up in the Weddell Gyre and eastward up to 150°E because of relatively warm and saline deep waters reaching the surface during the Weddell Sea polynya that occurs in the last 20 yr of the simulation. Anomalies associated with the occurrence of the Weddell Sea polynya are also noticeable in the biogeochemical tracer fields.

Except along Antarctic coasts, DIC and PO_4 concentrations south of 40°S are higher in the simulation, while

O_2 shows the opposite bias. The major reason for those biases seems to be an overexpression of the iron limitation in the modeled Southern Ocean (Galbraith et al. 2015, manuscript submitted to *J. Adv. Model. Earth Syst.*). The departure from observations may also be attributed to the (i) location of the wind-driven upwelling bringing tracers to the surface more equatorward in the simulation and (ii) observations being scarce and biased toward summer (that is low for DIC and PO_4 and high for O_2), in particular south of 60°S .

The ocean component of CM2.6 provides finescale circulation features such as boundary currents, interactions between jets and topography, and mesoscale eddy fields. However, because of time and computational constraints, the experimental design suffers from two main drawbacks: (i) the model is still drifting due to the relatively short length of the simulation and (ii) there was a lack of extensive evaluation and tuning of miniBLING during the development stage of the model. Running CM2.6 under a 1990 constant radiative forcing, Griffies et al. (2015) showed that the temperature drift was significantly reduced compared to previous coarser-resolution versions of the model, with drift reduction arising from the rich mesoscale eddy field in CM2.6. Moreover, one advantage of this brief simulation length is to prevent the physical and biogeochemical fields from drifting far away from the initial conditions. Finally, the fully prognostic implementation provides internally consistent physical–biogeochemical coupling. Hence, CM2.6–miniBLING provides an adequate framework in which to investigate the effect of finescale resolved processes, including mesoscale eddies, on physical and biogeochemical tracer transport.

b. Definition of ACC front paths

Fronts are boundaries separating regions of differing water mass characteristics. When these fronts have strong density gradients, they coincide with intense geostrophic currents, called jets, that tend to act as barriers to mixing. Traditionally, fronts have been identified using interior hydrographic properties (Orsi et al. 1995), but the advent of high-resolution satellite data has promoted the use of criteria based on sea surface temperature (SST) or sea surface height (SSH) to detect the associated jets (Gille 1994; Sokolov and Rintoul 2007; Sallée et al. 2008a). While defining fronts from hydrographic properties emphasizes their persistent nature as barriers between regions of different biophysical properties, defining them from dynamical properties highlights their variable nature as intense jetlike features steered by topographic obstacles. Among the various methods of front detection that have been developed over the last decades, we chose a “contour” method based on a hybrid fitting

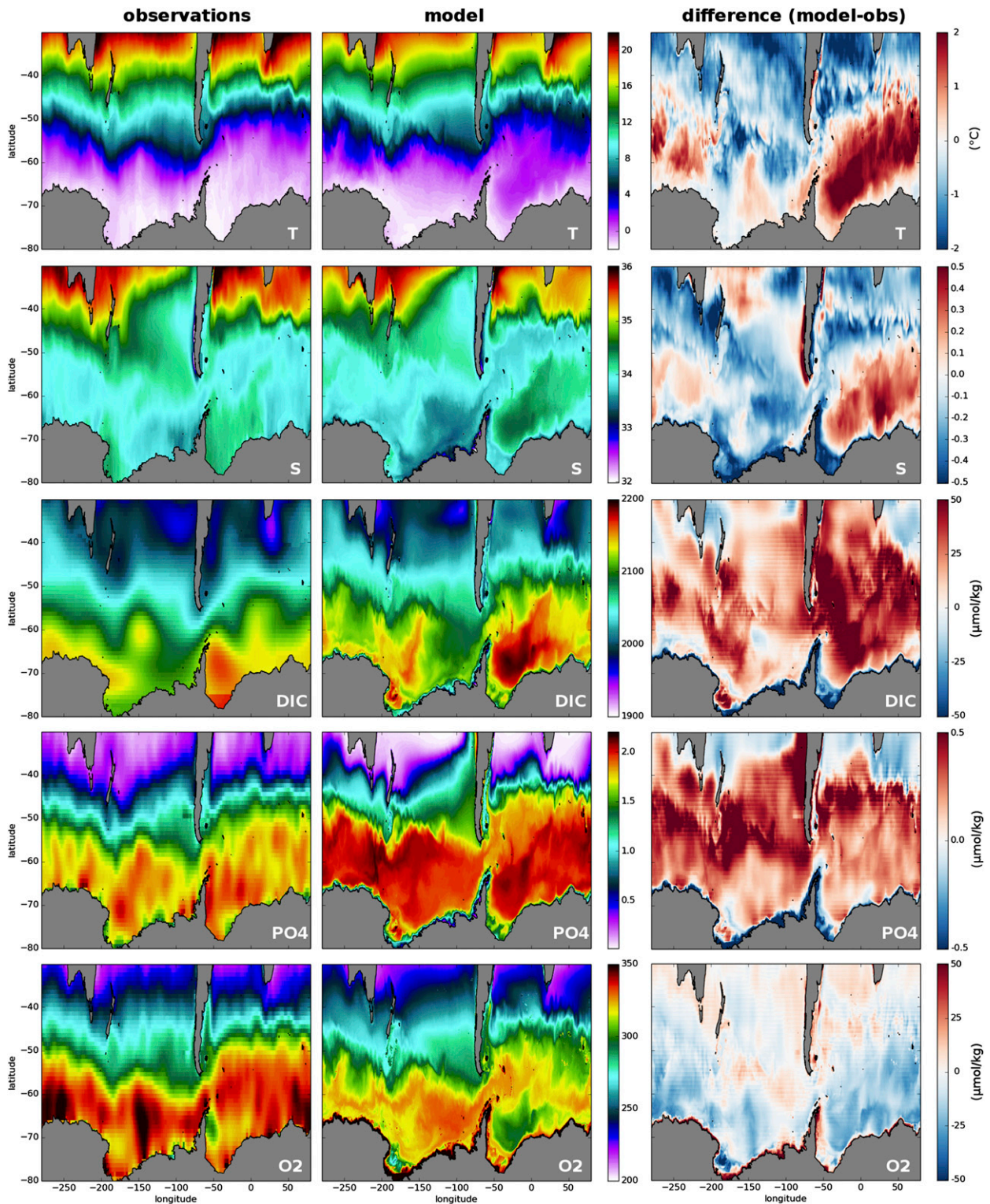


FIG. 2. Surface fields for (left) observations, (center) the average over the last 20 yr of the CM2.6-miniBLING simulation, and (right) the difference between the CM2.6-miniBLING simulation and observations. (top to bottom) Temperature ($^{\circ}\text{C}$), salinity, and DIC, PO₄, and O₂ (all $\mu\text{mol kg}^{-1}$). Observation fields of temperature, salinity, PO₄, and O₂ are from the *World Ocean Atlas 2009* (Locarnini et al. 2010; Garcia et al. 2010a,b) and DIC is from GLODAP corrected to preindustrial values (Key et al. 2004). These observational fields are the ones used to initialize the CM2.6-miniBLING preindustrial simulation and are thus interpolated onto the CM2.6 grid.

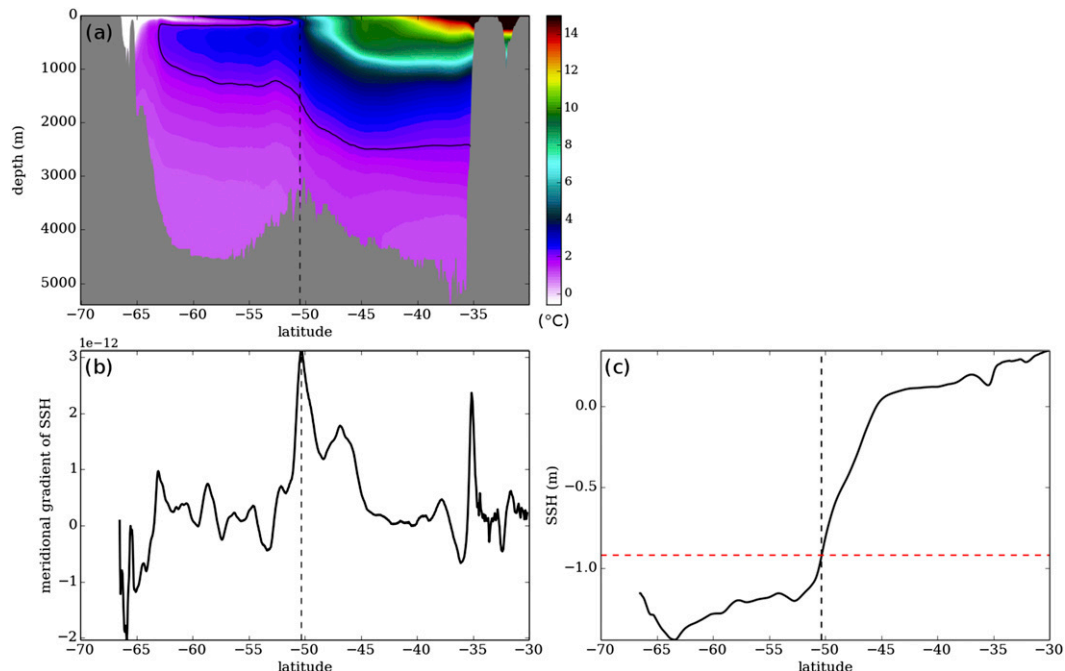


FIG. 3. Example of the front detection procedure for a meridional section at 115°E (corresponding to the I9 WOCE section). The 20-yr-averaged (a) temperature, (b) meridional SSH gradient, and (c) SSH. (a) The black solid contour corresponds to the 2°C isotherm. The black dashed line indicates the latitude matching the northernmost extent of AAWW and a local maximum of SSH meridional gradient. The red dashed line in (c) shows the SSH value (-0.92 m) corresponding to the latitude selected from (a) and (b). Note that this SSH value is specific to the meridional section at 115°E .

procedure (e.g., Sallée et al. 2008a; Dufour et al. 2011; Langlais et al. 2011; Dufour et al. 2013) that reconciles the hydrographic and dynamical views of the fronts (Langlais et al. 2011; Chapman 2014). More precisely, for each front the method identifies a single SSH contour based on hydrographic criteria (e.g., temperature and salinity) and dynamic criteria (e.g., transport and SSH gradients). For a review and comparison of the strength and weaknesses of the various jet detection methods, the reader is referred to Chapman (2014).

Our study will focus on one of the main fronts of the ACC, the PF, which shows strong horizontal property gradients and carries a significant part of the ACC transport. The transport of tracers across the SAF was also investigated in this study, leading generally to similar conclusions. Major differences between the two fronts will be briefly discussed in section 4.

The PF is usually defined as the location of the northernmost extent of Antarctic Winter Water (AAWW), identified by the 2°C isotherm at around 200-m depth (Belkin and Gordon 1996). We investigated 10 meridional sections (0°E , 30°E , 70°E , 115°E , 140°E , 170°E , 170°W , 90°W , 65°W , and 42°W) of the 20-yr average model fields, where these sections were taken at the position of several World Ocean Circulation Experiment

(WOCE) hydrographic lines (Orsi and Whitworth 2005). For each section, we identified a SSH value corresponding to the location of the PF from hydrography (temperature) and the most intense local meridional gradients of SSH (Fig. 3). This procedure provided 10 SSH values that were averaged to give the contour $\text{SSH}(\text{PF}) = -0.95\text{ m}$.

Though specific to our simulation, the SSH contour value found is consistent with previous modeling studies (e.g., Langlais et al. 2011). The front detection method was only applied to 10 meridional sections whose SSH contour values were then generalized to the circumpolar ocean by way of averaging. To check the generalization, we plotted the monthly climatology of the PF positions represented by the -0.95-m SSH contour on top of the lateral mean SSH gradients (Fig. 4). The seasonal positions of the PF show good agreement with intense local SSH gradients in most regions of the Southern Ocean. Mismatches are generally related to the SSH contour only following one of the several branches that form the PF as well as its inability to follow the splitting of the fronts that generally occurs downstream of topographic obstacles (e.g., Campbell Plateau). We note that the strong SSH gradients located north of the PF (e.g., at Campbell Plateau) correspond to the position of the

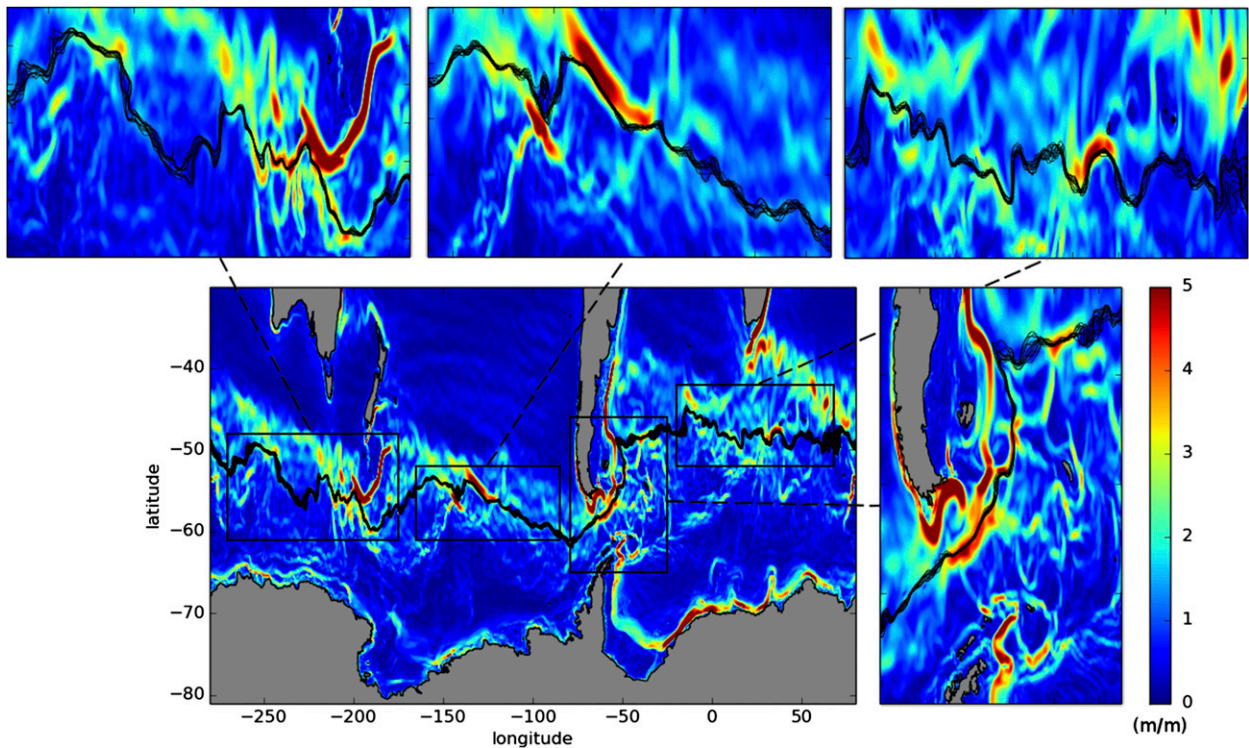


FIG. 4. Central panel shows the lateral gradients of 20-yr-averaged SSH ($|\nabla\overline{\text{SSH}}|$, colors, dimensionless), with red corresponding to intense $|\nabla\overline{\text{SSH}}|$, and 20-yr monthly climatology of the PF positions from the CM2.6–miniBLING simulation, with each black contour corresponding to a month. The PF position corresponds to $\text{SSH} = -0.95$ m. The exterior panels show close-up views of the central panel at various regions along the front.

SAF that carries most of the ACC transport in those regions (e.g., Sokolov and Rintoul 2007). Mismatches represent an inherent limitation of the contour method, which assumes that fronts are single well-defined circumpolar jets. Nonetheless, we need a circumpolar definition of fronts that represents their climatological position to calculate cross-frontal transport of tracers in the model. Moreover, this method allows us to link jets (which can suppress mixing) with fronts (which separate water masses), so that implications for heat, carbon, oxygen, and nutrients reservoirs can be more easily determined. SSH contours have also been shown to adequately represent both the mean path and mesoscale activity (meanders and eddies) of fronts, in particular the meridional deflection that fronts undergo when encountering a topographic obstacle (Langlais et al. 2011), and to be more suitable than other methods for high-resolution studies (Chapman 2014). Finally, we note that while the features of the cross-frontal tracer transport are independent of the choice of the variable (e.g., SSH, dynamic height anomaly) used to define the front position, the alongfront and depth-integrated cross-frontal tracer transport is sensitive to the exact path of the contour, as highlighted by Peña Molino et al. (2014).

c. Computation of cross-frontal transport components

1) METHOD

To compute mass (tracer) transport Φ across a section of a given front, meridional and zonal advective fluxes of mass (tracer) are integrated along the front (see appendix A for more details). The calculation is performed at every vertical level and bin of longitude in the model (i.e., at every 0.1° , which is the horizontal grid resolution).

Although the ACC fronts are known to be tightly steered by topography, their positions can vary in time, in particular in flat-bottomed areas or near topographic obstacles due to mesoscale activities or atmospheric forcing (Sallée et al. 2008a; Graham et al. 2012). Following Kwon et al. (2013), who reported the importance of accounting for the seasonal migration of density outcrops when computing subduction rates, the seasonal migration of fronts is accounted for in our calculation of the cross-frontal transport. To do so, a 20-yr monthly climatology of the PF position is created based on the 20-yr monthly climatology of the modeled SSH, using

the contour defined in section 2b [SSH(PF) = -0.95 m]. If we take January for example, this means that all the January transports are computed across the 20-yr January climatology of the front position, hence ensuring that the transport is not influenced by the climatological seasonal migration of the front. Figure 4 shows the monthly climatology of the PF position. While front paths are almost time invariant where fronts meet major topographic obstacles [e.g., Drake Passage (70°W) and Campbell Plateau (200°W)], they show more spatial variability upstream and downstream of these obstacles [e.g., downstream of Campbell Plateau or Kerguelen Plateau (70°E)] or where the bottom topography is flat [e.g., eastern Pacific abyssal plains (170°W) and Zapiola basin (40°W)], with a seasonal amplitude reaching ~5° of latitude in some places.

2) TRANSPORT COMPONENTS

Following Ballarotta et al. (2013), Bryan et al. (2013), and Griffies et al. (2015), we compute the mesoscale eddy component of the transport across a given front Φ_{eddy} for every month from

$$\Phi_{\text{eddy}} = \Phi_{\text{total}} - \Phi_{\text{mean}}, \quad (1)$$

where Φ_{total} is the total¹ component of the cross-frontal transport, and Φ_{mean} is its time-mean component. Let us take January once more as an example. To get Φ_{total} , we use the meridional and zonal advective fluxes of the tracers calculated online at every time step of the model and output at monthly period (see appendix A). Calculation of the transport from these online terms is done every January over the last 20 yr of the simulation. To get Φ_{mean} , we use advective terms computed offline from the 20-yr-averaged January output of tracer and velocity fields. Hence, Φ_{total} includes all the temporal correlations between tracer and velocity fields, while Φ_{mean} includes the temporal correlations between the 20-yr monthly climatologies of these fields. As a result, Φ_{eddy} includes all the temporal fluctuations departing from the 20-yr monthly mean climatology of cross-frontal transport. More details on this decomposition can be found in appendix B of Griffies et al. (2015).

Using this method, we are thus able to capture the variety of processes resolved in the model that contribute to the tracer transport across the climatological position of the fronts. Some of those processes can be observed on the daily snapshot of surface DIC south of Africa shown in Fig. 5, along with the mean position of

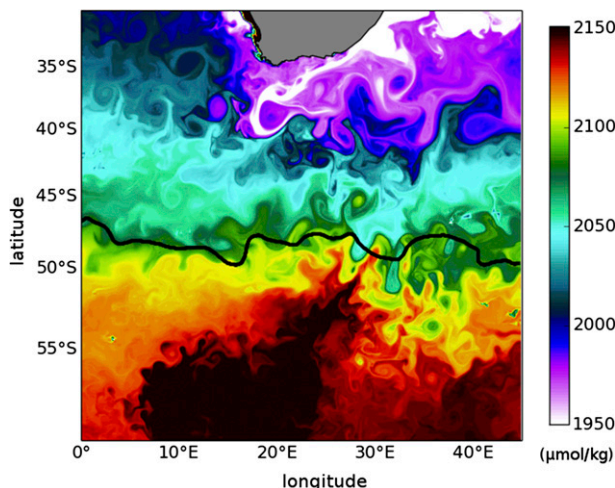


FIG. 5. The 20-yr-averaged position of the PF (black solid line) over a daily snapshot of surface DIC concentrations south of Africa. Note the variety of mesoscale features in the DIC field, including rings detaching from the front edge and finescale meandering of the DIC field around the climatological front position.

the PF. Tracer and velocity anomalies at the climatological front position that result from instantaneous fluctuations of the front, rings detaching from the front edges, or waves propagating across the fronts are all accounted for in the cross-frontal transport calculation and fall into the mesoscale eddy component Φ_{eddy} . Hence, mesoscale eddies should be understood here in the broad sense of transient mesoscale activity (meanders, rings, waves, etc.). More details on the kinematic interpretation of transport across a climatological front position can be found in appendix A.

d. Representation of fronts in the vertical

In the following, we use potential density referenced to 2000 m (σ_2) to bin tracers and transports (see appendix B) and to define the vertical extension of the jets as well as the Ekman layer. The quantity σ_2 is preferred over depth as it is more consistent with water mass properties and over σ_1 , as we generally display results for the whole water column. This choice also has the advantage of comparability with the many other modeling studies that use σ_2 when investigating transport binned into density layers (e.g., Lee et al. 2007; Ballarotta et al. 2013).

Though jets are deep reaching in the Southern Ocean, sometimes extending down to the ocean floor (e.g., Graham et al. 2012), intense jets are mostly confined to the upper 1–1.5 km (Smith and Marshall 2009; Abernathy et al. 2010), and thus generally lie above the sill of major topographic obstacles (~2 km; see Fig. 6). At these depths and where the jet is unbounded, Ekman transport and

¹ In the following, total is used for the sum of the time-mean and eddy components, while net is used for the sum of northward and southward transports.

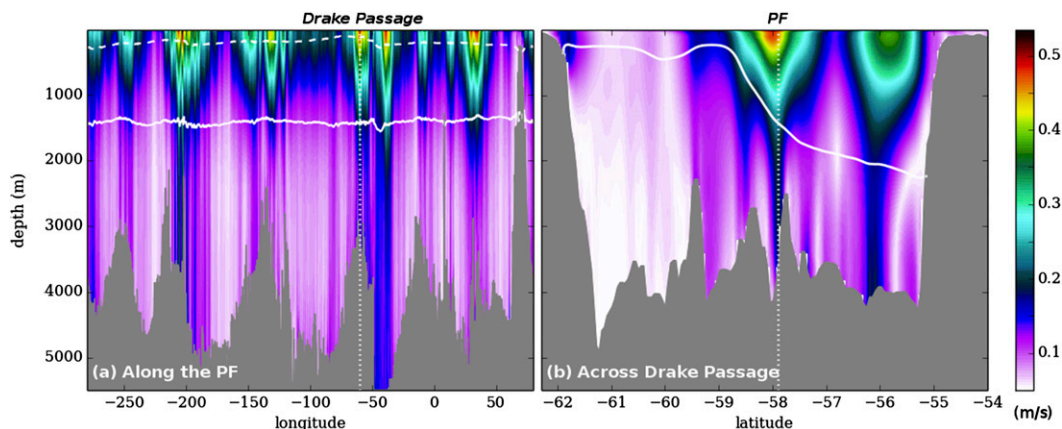


FIG. 6. The 20-yr-averaged current speed (m s^{-1}) from the CM2.6–miniBLING simulation (a) along the path of the PF and (b) across Drake Passage at 60°W . The solid white line shows $\sigma_2 = 36.9 \text{ kg m}^{-3}$, the isopycnal chosen as the lower boundary of the PF core, with σ_2 the potential density referenced at 2000 m. (a) The white dashed line shows $\sigma_2 = 36.4 \text{ kg m}^{-3}$, the isopycnal chosen as the lower boundary of the Ekman layer (see section 2d for further details). The vertical white dotted lines correspond to the location of (a) Drake Passage (60°W) and (b) the PF. Note that the jets are only intense in some locations, as also visible in Fig. 4.

mesoscale eddies are the main conveyers of tracer transport across the front. The lower boundary of the front core is thus defined here as the depth that lies just above the deep southward geostrophic transport, which is restricted to below the sill of major topographic obstacles. Based on the time-mean component of the mass transport across the PF binned into σ_2 coordinates (Fig. 7c1, blue line), $\sigma_2 = 36.9 \text{ kg m}^{-3}$ is chosen as the deepest extension of the PF core (Figs. 6 and 7c1, solid lines). Though the ocean is weakly stratified in this density range, meaning that a small change in σ_2 corresponds to a large change in depth, we note that our conclusions are not very sensitive to the σ_2 value chosen (e.g., $\sigma_2 = 37.0 \text{ kg m}^{-3}$ would give very similar results). Figure 6 shows that $\sigma_2 = 36.9 \text{ kg m}^{-3}$ delimits the vertical extension of the intense jets that form the model PF and that lie above the sill of major topographic obstacles at a depth of around 1.5 km, in agreement with observations (e.g., Smith and Marshall 2009). We note however that the model PF intersects topography above 36.9 kg m^{-3} at the Kerguelen Plateau ($\sim 70^\circ\text{E}$), inducing a weak geostrophic transport within the PF core as we will see in section 3.

Previous studies have reported that while transport is inhibited across the core of the jet, the Ekman layer remains a region of vigorous cross-frontal transport (e.g., Palter et al. 2013). To investigate the role of various transport components in the cross-frontal transport of tracers, we divided the frontal core region into two layers, corresponding to the Ekman layer and below the Ekman layer, that is, from the base of the Ekman layer down to the lower boundary of the front core. Based on the total component of the mass transport across the PF

binned into σ_2 coordinates (Fig. 7c1, black line), $\sigma_2 = 36.4 \text{ kg m}^{-3}$ is chosen as the deepest extension of the Ekman layer (Figs. 6a and 7c1, dashed lines). The $\sigma_2 = 36.4 \text{ kg m}^{-3}$ delimits the near-surface layer where the total transport is primarily driven by the time-mean transport (Fig. 7c1, blue line), that is, mostly by the Ekman transport. In the model, the alongfront average depth of $\sigma_2 = 36.4 \text{ kg m}^{-3}$ ranges from around 140- to 200-m depth over the seasons. As our cross-frontal transport calculation captures the seasonal cycle (section 2c), the transport we compute is expected to be carried within different density ranges in different seasons. The $\sigma_2 = 36.4 \text{ kg m}^{-3}$ thus corresponds to the densest waters lying within the winter Ekman layer. Finally, we note that the σ_2 chosen to define the lower boundaries of the Ekman layer and the jet core are specific to the PF.

3. Results

a. Eddy contribution to cross-frontal tracer transport

We start our analysis by investigating the net (i.e., sum of northward and southward transports) effect of eddies on the total (i.e., sum of the time-mean and eddy components) transport of tracers across the PF core. We then explore the regions where the cross-frontal transport is favored and investigate the importance of these regions for the net transfer of tracers across the PF. In the following, results are presented in the three layers defined in section 2d, that is, (i) the entire core of the PF, subdivided into (ii) the Ekman layer, and (iii) below the Ekman layer.

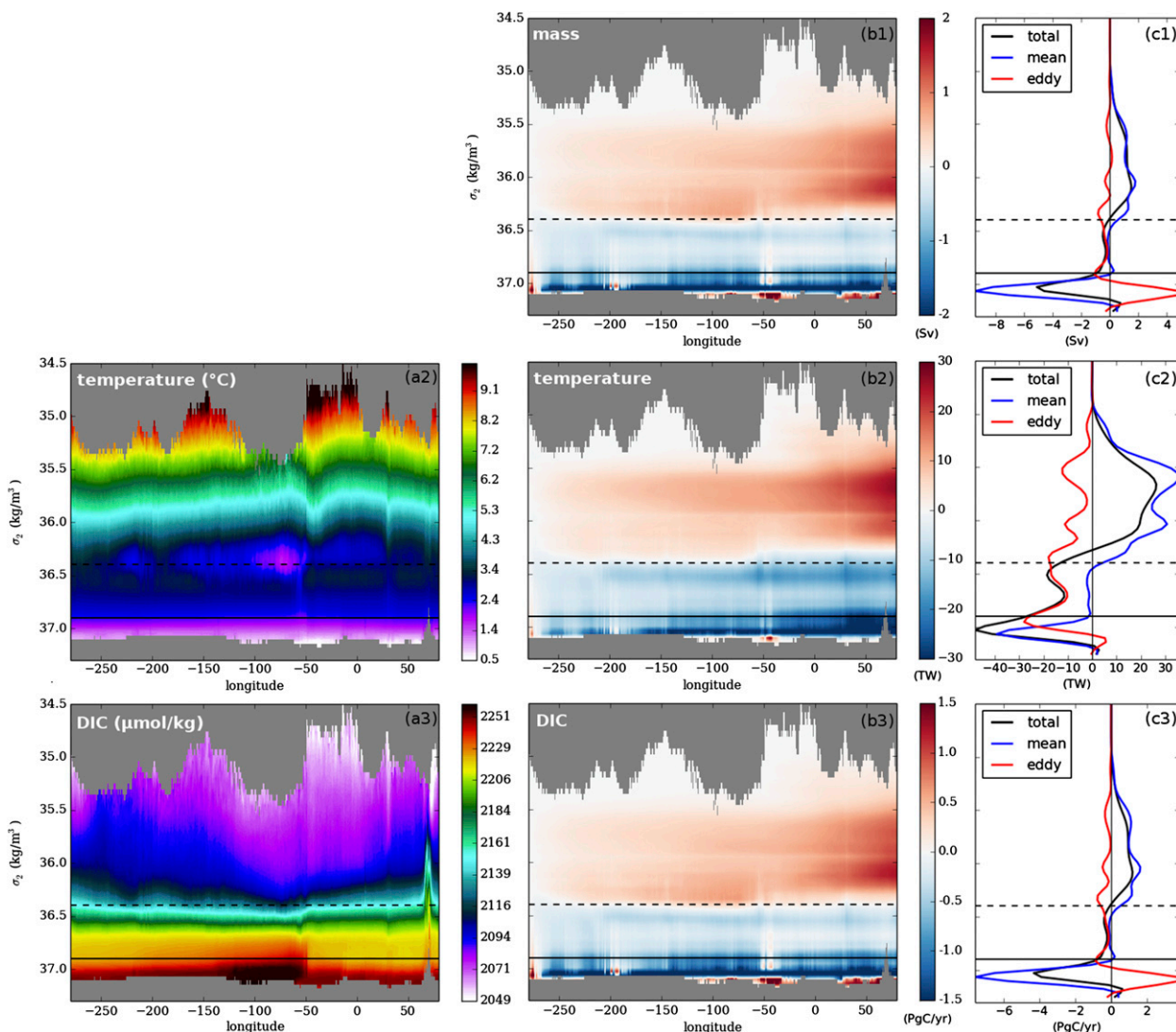


FIG. 7. The 20-yr-averaged tracer distributions and transports across the PF against σ_2 . (a) Temperature and DIC along the PF binned into σ_2 layers. (b) Mass, temperature, and DIC transports across the PF cumulatively summed along the front for every σ_2 layer. (c) Mass, temperature, and DIC transports across the PF summed along σ_2 layers with the total transport (black) deconvolved into its time-mean component (blue) and transient eddy component (red). Transport scales are dependent on the size of σ_2 bins. The reader is thus referred to Fig. 8 to get a sense of how large the transports are. Positive transports are northward. Temperature transport ($\text{Sv } ^\circ\text{C}$) is expressed as heat transport equivalent in TW. Vertical profiles have been smoothed with a low-pass filter. This results in different minima and maxima in the transports of (b) and (c). The black dashed line marks the base of the Ekman layer ($\sigma_2 = 36.4 \text{ kg m}^{-3}$) and the black solid line the lower extension of the PF core ($\sigma_2 = 36.9 \text{ kg m}^{-3}$). Details of how the limits of the PF core and the Ekman layer are chosen are provided in section 2d.

1) THE BALANCE OF TRANSPORT COMPONENTS ACROSS THE PF

Figure 7 shows the 20-yr average of temperature and DIC fields along the PF (Fig. 7a) and the mass, temperature, and DIC transports across the PF as a cumulative sum (Fig. 7b) or sum (Fig. 7c) along the front. Each transport is binned into σ_2 layers along the path of the PF. By definition (section 2d), the

total cross-frontal transport is mainly northward in the Ekman layer and southward below. Below the PF core ($\sigma_2 \geq 36.9 \text{ kg m}^{-3}$, horizontal black line in Fig. 7), a geostrophic current transports deep waters southward, providing a net flux of heat, carbon, oxygen, and nutrients to high latitudes. A weak geostrophic current transports AABW northward in the deepest σ_2 layers (Figs. 7b,c), allowing for a northward flux of tracers into the abyss.

We now return to the PF core ($\sigma_2 \leq 36.9 \text{ kg m}^{-3}$), the region of our focus. Within the Ekman layer, the cross-frontal transport of mass is northward and is driven by the time-mean component, that is, mainly the Ekman transport, with some compensation from eddies (Fig. 7c1). Below the Ekman layer and down to the bottom of the PF core, the cross-frontal transport is mainly southward and weaker than in the Ekman layer. Here, the eddy component is the main driver of the total cross-frontal transport, with little contribution from the time-mean component. This eddy-driven regime that lies between the Ekman-driven and geostrophy-driven regimes is consistent with the traditional zonally averaged picture of momentum balance at the latitudes of Drake Passage (e.g., Olbers et al. 2004; Marshall and Speer 2012). Departure from this balance mainly involves the incursion of geostrophic transports into the eddy-driven regime. We identify two main sources of geostrophic transports within the PF core: the intersection of the PF core with the Kerguelen Plateau (Fig. 6a) and the deviation of the mean flow from the surface flow with depth (see next section). Another source of geostrophic transports might arise from the intersection of some PF core isopycnals with the ocean surface as discussed in Mazloff et al. (2013). Transports look quite different when averaged along latitude circles instead of along the front (see Fig. 1b). As Treguier et al. (2007) showed, calculating the transport across mean streamlines rather than latitude circles more effectively reveals the physical nature of the meridional overturning in the upper ocean. In particular, averaging along streamlines removes the effect of stationary meanders that show a large contribution to the transport averaged along latitude circles (e.g., Treguier et al. 2007; Dufour et al. 2012). Though our frontwise SSH coordinate does not correspond to streamlines, it provides a proxy for the flow path with the best agreement being at the surface (i.e., the SSH contour follows the surface geostrophic flow).

Similarities in Fig. 7b show that temperature and DIC cross-frontal transports are closely following mass transport (see also Fig. 9). As temperature and DIC advective transports have the same sign as mass transport, those similarities suggest that eddy-diffusive transport either reinforces the advective transport or is small enough so that it does not change the sign of the transport. This point will be further discussed in section 3b. However, Figs. 7c1–c2 reveals that the alongfront sum of cross-frontal temperature transport differs significantly from that of mass. The key difference is that temperature transport is enhanced in the upper layers. In contrast, the alongfront sum of cross-frontal DIC transport is very similar to that of mass (Figs. 7c1,c3), as are the alongfront

sum of cross-frontal PO_4 and O_2 transports (not shown). Differences between cross-frontal transport of temperature and biogeochemical tracers arise from the vertical gradient of temperature [$(\partial\Theta/\partial\sigma_2)/\Theta_{\min}$; Fig. 7a2] being around 10 times greater than that of biogeochemical tracers [e.g., $(\partial\text{DIC}/\partial\sigma_2)/\text{DIC}_{\min}$; Fig. 7a3] because of the temperature transport being expressed in degrees Celsius (see appendix A).

Figure 8 presents an integrated view of the cross-frontal transports of Fig. 7c for mass and the four tracers, here partitioned into the three layers defined in section 2d. Within the PF core, the sum of the total cross-frontal transport is northward for all tracers. This transport is a result of (i) strong northward transport in the Ekman layer, dominated by Ekman transport with partial compensation from the eddy component, and (ii) a more modest (~ 4 times smaller) southward transport below the Ekman layer, dominated by eddy transport with very little contribution from the time-mean geostrophic transport as noted in Fig. 7c. Thus, transport across the PF core is dominated by the northward Ekman flow, with eddies providing a significant southward transport that drives the total transport below the Ekman layer. The imbalance between the northward time-mean transport and the southward eddy transport in Fig. 8 indicates that the upper cell of the MOC is mostly closed below the PF core. Eddy transports are found to provide around 40% of the southward flow that closes the upper cell and to be located primarily above the sill depth of major topographic ridges. The remaining ($\sim 60\%$) is provided by geostrophic transports. This result contrasts with the more traditional picture of an upper cell mostly closed by eddy transports above topographic ridges, as conveyed in particular by idealized studies or tracer inversion [e.g., Lumpkin and Speer (2007); see also the review of Marshall and Speer (2012)]. However, we note that our result is consistent with Mazloff et al. (2013).

Over the entire depth of the PF, we estimate that eddies support around one-third of the southward mass transport with the remaining two-thirds being supported by geostrophic currents. Eddies are also found to support more than two-thirds of the southward temperature transport, with more than 80% achieved within the PF core. This predominance of eddies in transporting temperature southward with weak but significant contribution from geostrophic currents is in agreement with previous observational and modeling studies (e.g., de Szoek and Levine 1981; Peña Molino et al. 2014).

2) HOTSPOTS OF TRACER TRANSPORT

The alongfront spatial variability in the cross-frontal transport is shown in Fig. 9. Here, we show the topography in the model (Fig. 9a) and the 20-yr-averaged

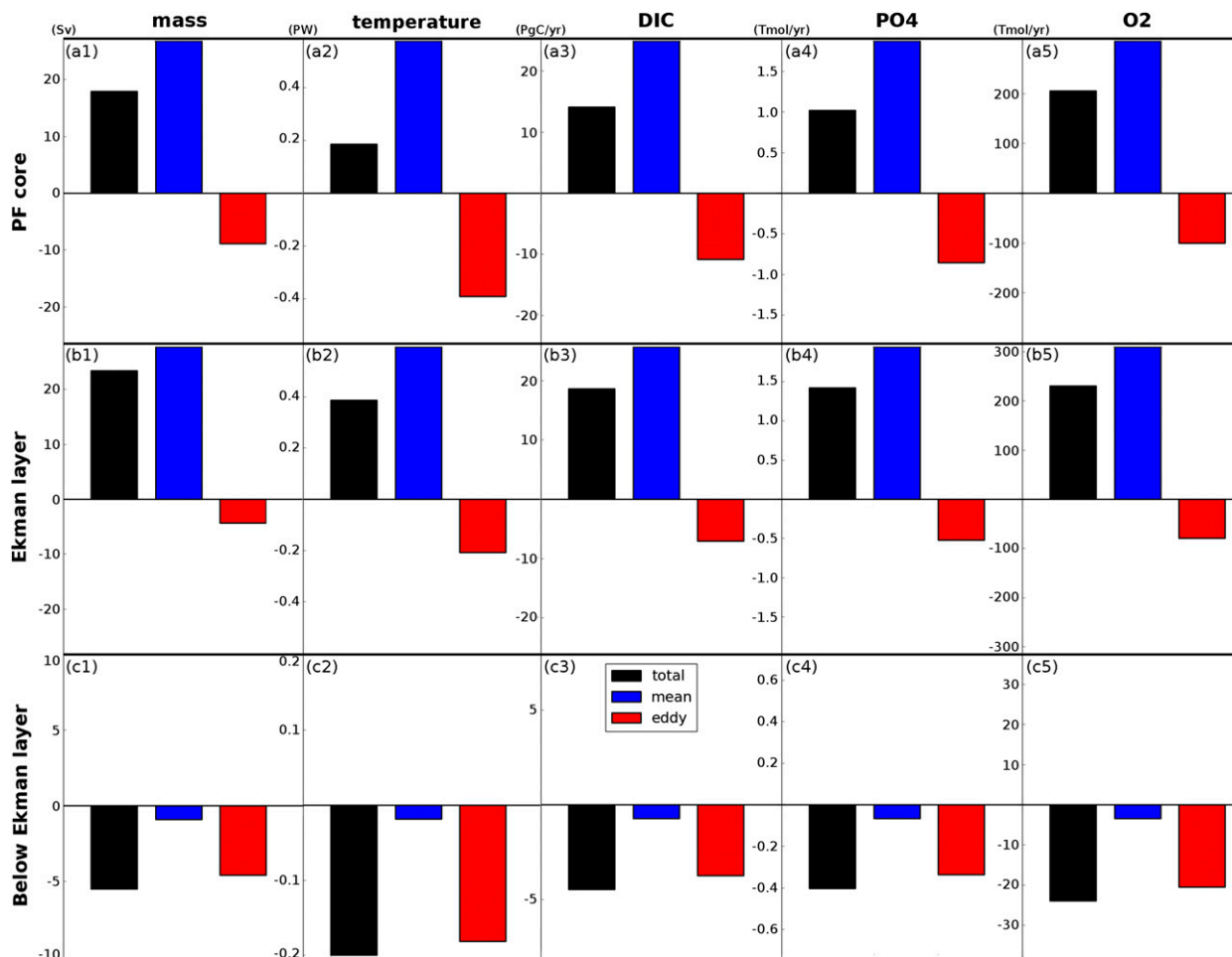


FIG. 8. The 20-yr averages of the transport of mass, temperature, DIC, PO_4 , and O_2 across the PF, horizontally integrated along the PF and vertically integrated within (a) the PF core ($\sigma_2 \leq 36.9 \text{ kg m}^{-3}$), then separated into the (b) Ekman layer ($\sigma_2 \leq 36.4 \text{ kg m}^{-3}$), and (c) below the Ekman layer ($36.4 \text{ kg m}^{-3} < \sigma_2 \leq 36.9 \text{ kg m}^{-3}$). Note the difference in scales between (c) and (a) and (b). Details of how the limits of the PF core and the Ekman layer are chosen are provided in section 2d. The total transport (black) is deconvolved into its time-mean component (blue) and its transient eddy component (red). Positive transports are northward. Temperature transport (Sv $^\circ\text{C}$) is expressed as heat transport equivalent in PW.

components of the transport across the core of the PF ($\sigma_2 \leq 36.9 \text{ kg m}^{-3}$) at every 0.1° of longitude (Fig. 9b) for mass, temperature, and DIC. Both time-mean and eddy components are enhanced where the front encounters major topographic obstacles, namely, at the Southeast Indian Ridge, Campbell Plateau, Macquarie Ridge, East Pacific Rise, Drake Passage, Mid-Atlantic Ridge, Southwest Indian Ridge, and Kerguelen Plateau (Fig. 9b). The PO_4 and O_2 transports exhibit very similar features (not shown) to that of mass and DIC transports in these hotspots. At every 0.1° of longitude, the time-mean component drives a large part of the total transport across the PF, with the eddy component being less than 20% of the time-mean component (Fig. 9b). This feature holds for mass and biogeochemical tracers but not for

temperature, whose eddy component shows amplitudes twice as large as those for mass and DIC. Despite the minor local contributions of the eddy component, when transport is summed along the PF, the eddy contribution to the total cross-frontal transport is of the same magnitude as its time-mean counterpart, as noted in Fig. 8.

Any advective flux contains rotational and divergent components (e.g., Marshall and Shutts 1981; Roberts and Marshall 2000; Fox-Kemper et al. 2003; Bishop 2013). However, there is no unique decomposition of such a flux into rotational and divergent components (Fox-Kemper et al. 2003). Although we do not attempt to perform such a decomposition here, we infer a non-trivial rotational component in regions of active eddies, such as near topography. In Fig. 9b, the cross-frontal

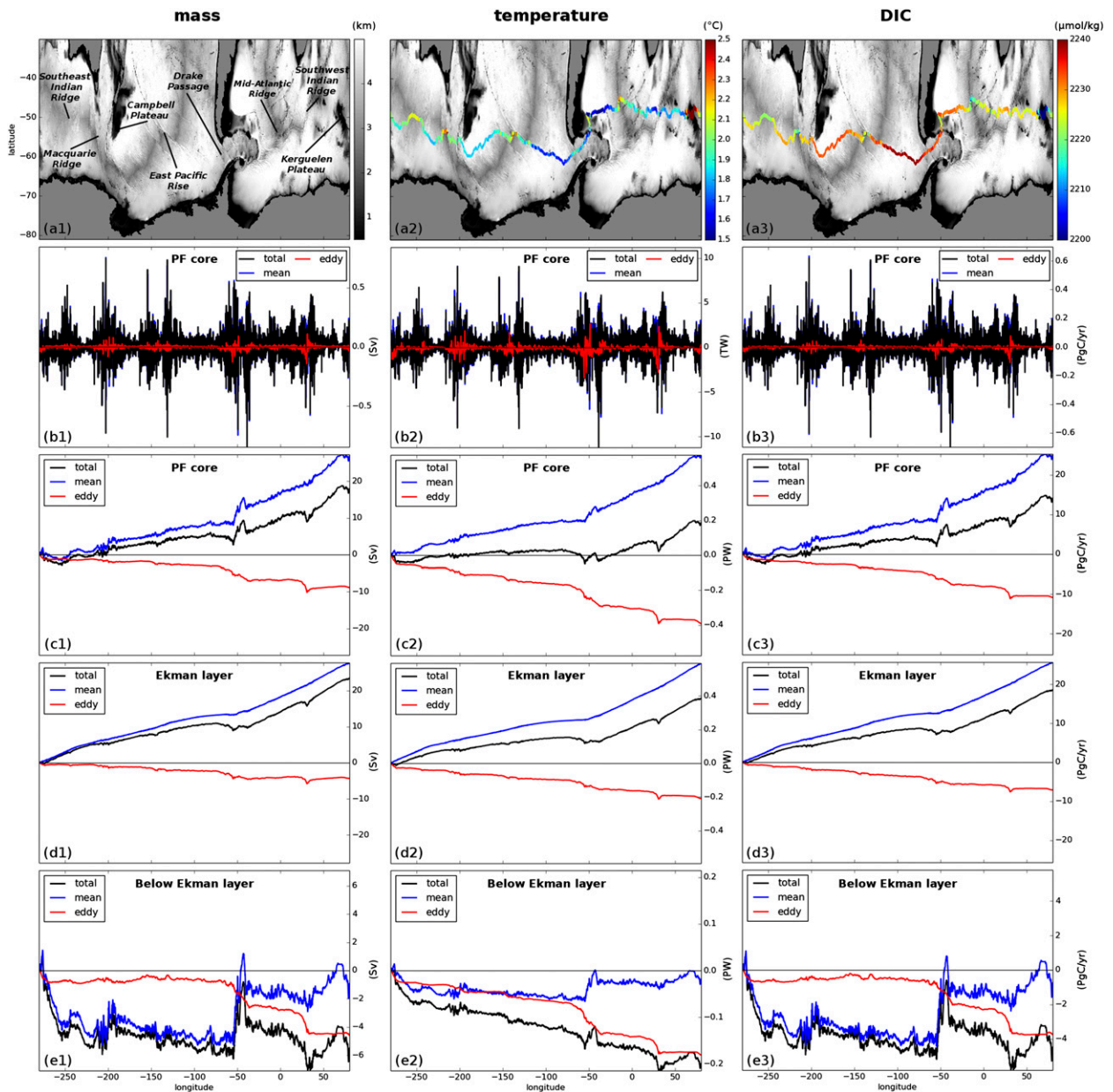


FIG. 9. Geographic distribution of cross-frontal transport of mass, temperature, and DIC. (a) Model topography (background black and white) and (a2), (a3) 20-yr-averaged tracer at the PF (colored contours). Tracers in (a2)–(a3) are averaged vertically between the surface ocean and the lower extension of the PF core ($\sigma_2 \leq 36.9 \text{ kg m}^{-3}$). (b) The 20-yr-averaged transport across the PF at every 0.1° of longitude. The 20-yr-averaged transport across the PF cumulatively summed along the front. The total transport (black) is deconvolved into its time-mean component (blue) and its transient eddy component (red). Transports are integrated vertically between (c) the surface ocean and the lower extension of the PF core ($\sigma_2 \leq 36.9 \text{ kg m}^{-3}$) and then separated into (d) the Ekman layer ($\sigma_2 \leq 36.4 \text{ kg m}^{-3}$) and (e) below the Ekman layer ($36.4 \text{ kg m}^{-3} < \sigma_2 \leq 36.9 \text{ kg m}^{-3}$). Note the difference in scales between (c), (d) and (e). Details of how the limits of the PF core and the Ekman layer are chosen are provided in section 2d. Positive transports are northward. Temperature transport ($\text{Sv } ^\circ\text{C}$) is expressed as heat transport equivalent in PW.

transport indeed exhibits rather large fluctuations at hotspots. Integrating over a portion of the front allows some cancellation of the rotational component, though the rotational component cannot be perfectly removed by way of averaging (Griesel et al. 2009). Here, we

investigate the divergent component of the cross-frontal transport by computing the alongfront cumulative sum of the cross-frontal transport in the three layers (Figs. 9c–e). Note that when integrating around Antarctica, the rotational component of the flux vanishes (integral along a

closed contour) so that the sums presented in Figs. 8 and 9 correspond to the divergent part of the flux only.

In the Ekman layer (Fig. 9d), the time-mean component displays a smooth positive slope, reflecting the Ekman flow that drives northward cross-frontal transport all along the PF, consistently exporting waters and their tracer content northward. Below the Ekman layer (Fig. 9e), the time-mean component shows large fluctuations that intensify where the PF flows around major topographic obstacles (e.g., Campbell Plateau and Drake Passage). Large fluctuations in the time-mean component of the cross-frontal transport mainly result from a lack of alignment between the mean flow and the SSH contour used to define the front. Deviations of the mean flow from the surface flow have been shown to increase with depth and to be enhanced where the front develops large meanders due to interaction with topography (Peña Molino et al. 2014; Phillips and Bindoff 2014). This deviation is a result of the ACC being non-equivalent barotropic (i.e., deep flow not parallel and not proportional to the surface flow). Deviations of the mean flow are known to support a significant transport across the front (Peña Molino et al. 2014). For instance, in the Ekman layer, the time-mean mass transport across the PF (27.7 Sv; Fig. 8b1) results from a northward transport of 32.1 Sv by the Ekman flow and a poleward transport of 4.4 Sv by deviations of the mean geostrophic flow from the surface flow. This mean geostrophic cross-frontal transport results from the near cancellation between large zonal and meridional components [$O(50)$ Sv].

We now examine the divergent component of the cross-frontal transport for the eddy component. The eddy component shows a marked steplike behavior in each layer (Figs. 9c–e), indicating that the eddy transport is strongly enhanced at and near major topographic obstacles (i.e., at hotspots of tracer transport) and very small elsewhere. This behavior of the eddies contrasts to the time-mean component, which contributes to the total cross-frontal transport all along the PF. Intensification of the eddy component thus occurs in the vicinity of major topographic obstacles where the mean flow is strong and meandering, as shown by both the intense mean current speed (Fig. 6) and sharp lateral gradients of SSH (Fig. 4). Naveira Garabato et al. (2011) hypothesized the link between regions of large mean flow strain and hotspots of transport or leaky jet segments in the ACC. In such regions where large-scale standing meanders develop, baroclinicity of the mean flow is increased through topographic steering, leading to enhanced baroclinic instability that intensifies eddy-advective activity (Thompson and Sallée 2012). Topographic

steering of the mean flow also sharpens the cross-frontal tracer gradient as the jet narrows, potentially increasing the eddy-diffusive activity. Finally, standing meanders distort the front meridionally, increasing the surface of exchange at the front. These ideas have been hypothesized or discussed in several recent studies, which all tend to show that eddy activity is augmented in the presence of standing meanders (Naveira Garabato et al. 2011; Thompson and Sallée 2012; Zika et al. 2013; Abernathey and Cessi 2014). In particular, using numerical simulations with and without topography, Abernathey and Cessi (2014) showed that cross-frontal eddy heat flux was stronger in the experiment with topography due to the presence of standing meanders.

3) EFFECT OF HOTSPOTS ON THE TOTAL TRANSPORT

In between topographic obstacles, the time-mean component dominates the total transport driving a northward transport, as indicated by the smooth positive slope in Fig. 9c. At major topographic features, the southward eddy transport intensely opposes the Ekman transport, thus reducing the net northward cross-frontal transport or driving a net southward transport, as highlighted by the steplike features in Fig. 9c. In particular, the total transport displays strong southward deflections downstream of Drake Passage, Kerguelen Plateau, and the Southwest Indian Ridge. In these regions where the PF encounters large topographic obstacles, intense eddy activity has been reported (e.g., Meredith and Hogg 2006; Morrow et al. 2010). Drake Passage is where the PF develops its largest meridional excursion, leading to increased baroclinic instability and a large surface of exchange across the front, two conditions that favor increased eddy contribution. At the Southwest Indian Ridge, observational studies have reported the presence of a warm eddy corridor that allows some eddies to cross the PF and transport heat to the Antarctic zone (e.g., Gouretski and Danilov 1994; Ansong et al. 2014).

Hence, our diagnostics show that eddies induce a southward cross-frontal transport of tracers all along the PF, partially compensating the northward Ekman transport in the Ekman layer and dominating the total transport in the PF core below the Ekman layer. At major topographic obstacles, however, the enhanced eddy activity drives a southward total cross-frontal transport throughout the PF core. Hence, we conclude that it is in the regions between topographic obstacles that upwelled water or tracers are returned to the north. In contrast, hotspots are privileged pathways for the transport of water and tracers to the south.

b. Advective versus diffusive role of eddies

Eddies act to move tracers along isopycnals via two mechanisms: eddy-advective transport [also called the [Gent and McWilliams \(1990\)](#) effect], resulting from extraction of available potential energy from the unstable mean flow, and eddy-diffusive transport (also called isopycnal or neutral diffusion), resulting from eddies stirring tracers along isopycnals to be eventually mixed by small-scale processes. While the eddy tracer diffusive transport is downgradient in steady state, the eddy tracer advective component can be either upgradient or downgradient, depending on the large-scale tracer distribution with respect to dynamical circulation. Hence, eddy-advective and eddy-diffusive transports can either reinforce or oppose each other. Here, we compare eddy cross-frontal transport for mass, temperature, DIC, PO_4 , and O_2 and provide a scaling of the eddy-diffusive transport for each tracer to infer the relative importance of eddy-advective and eddy-diffusive transports.

1) COMPARISON OF EDDY CROSS-FRONTAL TRANSPORTS BETWEEN TRACERS

As seen in [Fig. 8](#), all tracers present the same general picture as mass. That is, for each layer, the balance between transport components is similar in terms of sign and relative magnitude. The eddy components of the cross-frontal transport of mass and tracers also present very similar features, both regarding spatial patterns (i.e., transports increase/decrease at the same locations) and sign (i.e., transports oppose/reinforce the time-mean component; see [Figs. 7](#) and [9](#)). Considering that mass is only advected (no diffusion), these similarities suggest that eddy-diffusive transport is negligible or alternatively that eddy-diffusive and eddy-advective transports reinforce each other. In the following, we explore these two scenarios.

Despite similarities in the eddy components of mass and tracer transports, [Fig. 8](#) shows that the degree to which eddies oppose the time-mean transport varies significantly between mass and tracers as well as among tracers (see also [Figs. 7](#) and [9](#)). There are two ways for the ratio of the eddy to the time-mean transport of tracers to differ from that of mass. First, the spatial distribution of the tracers may increase the contribution from one transport component over the other. If tracers were uniformly distributed in the ocean, the ratio would be the same for mass and the tracers. However, tracers have nonuniform alongfront and vertical distributions ([Figs. 7a, 9a](#)), and time-mean and eddy components are predominant at different locations and depths, so that the ratio is likely to be different between mass and

tracers as well as between tracers. For instance, tracers whose concentration decreases with depth, like temperature and O_2 , are likely to have a lower ratio than tracers whose concentration increases with depth, like DIC and PO_4 , because time-mean transport across the PF core is only large in the Ekman layer. Second, the ratio can vary between mass and tracers because the cross-frontal isopycnal tracer gradient may support an eddy-diffusive transport that either opposes or reinforces the eddy-advective transport. If the tracers were uniformly distributed on the isopycnals, eddy-diffusive transport would be zero so that the eddy-advective component would be the only contributor to eddy transport, as is the case for mass.

2) ALONG-ISOPYCNAL TRACER GRADIENTS

Several studies have proposed a simple rule to determine the direction of eddy-diffusive transport by examining the relative slopes of tracers and isopycnals (e.g., [Gregory 2000](#); [Lee et al. 2007](#)). [Figures 10a1–d1](#) shows temperature, DIC, PO_4 , and O_2 binned in (SSH ; σ_2) space in the region of the PF. At the PF, temperature is generally warmer in the light layers and cooler in the deep layers but shows an inversion between 36.2 and 36.6 kg m^{-3} , which is the signature of cold and fresh AAWW extending from the south to the PF ([Fig. 10a1](#)). DIC concentrations increase with depth ([Fig. 10b1](#)), as do PO_4 concentrations except between 36.5 and 36.7 kg m^{-3} , where a local maximum of PO_4 lies just above a local minimum ([Fig. 10c1](#)). Finally, O_2 concentrations decrease with depth except in the density range of the PO_4 maximum where O_2 shows a local minimum ([Fig. 10d1](#)). These local extrema correspond to the nutrient-rich and oxygen-poor UCDW and the nutrient-poorer LCDW, respectively, in agreement with observations (e.g., [Orsi and Whitworth 2005](#)).

Comparing the relative slopes of tracer isosurfaces and isopycnals, we note that the isotherms are generally steeper than isopycnals, in particular between around 36.2 and 36.7 kg m^{-3} , indicating that the cross-frontal isopycnal temperature gradient is intense in these layers ([Fig. 10a1](#)). In contrast, biogeochemical tracer isosurfaces are closely aligned with isopycnals below 36.2 kg m^{-3} , indicating weak cross-frontal isopycnal gradients ([Figs. 10b1–d1](#)). This close alignment holds in particular for DIC and PO_4 , while O_2 isosurfaces show significant slopes between 36.0 and 36.5 kg m^{-3} . The steepness of isotherms relative to isopycnals is typical of the Southern Ocean, where density is partly controlled by salinity and the vertical gradient of temperature is relatively weak, leading to a northward along-isopycnal temperature gradient ([Gregory 2000](#)). The close alignment between biogeochemical tracer isosurfaces and

isopycnals results from the combined effects of (i) the action of the biological pump, which tends to stratify the biogeochemical tracer concentrations, and (ii) the circulation, which, as it tilts isopycnals in the Southern Ocean, tilts the biogeochemical tracer surfaces as well. Hence, in the ocean interior, the weak along-isopycnal gradients of biogeochemical tracers may reflect the importance of circulation over local sources and sinks.

3) SCALING OF EDDY-DIFFUSIVE TRANSPORT

Considering the close alignment between biogeochemical tracer isosurfaces and isopycnals, an additional diagnostic is needed to investigate further the eddy-diffusive transport. A rough scaling of eddy-diffusive transport for tracers χ_C across the front and on an isopycnal layer can be computed as follows (e.g., Griffies 2004, his section 6.11):

$$\chi_C = -\rho_0 \kappa \bar{h} (\nabla \bar{C}) \cdot \mathbf{n} dl, \quad (2)$$

where $\kappa > 0$ is a coefficient of along-isopycnal eddy diffusivity, h is the isopycnal thickness, C is the tracer concentration, dl is the front segment, \mathbf{n} is the vector normal to dl , and the overbar denotes a 20-yr average over a given month. However, given the simple approach of Eq. (2), we cannot accurately infer the eddy tracer advective transport by subtracting χ_C from the eddy component shown in Fig. 8. Rather, this scaling allows us to examine the sign and strength of the along-isopycnal tracer gradients as a contributor to the eddy-diffusive transport and to compare the magnitude of eddy-diffusive transport estimates between the various tracers.

The tracer gradient contribution to the eddy-diffusive transport is shown in Figs. 10a2–d2. Along-isopycnal tracer gradients across the PF are integrated along the PF and within isopycnal layers and multiplied by -1 [see Eq. (2)]. Thus, the sign of the eddy-diffusive transport can also be examined. The eddy-diffusive transport is southward in all layers for temperature (Fig. 10a2), while being mainly southward for DIC and northward for O_2 (Figs. 10b2,d2). Eddy-diffusive transport for PO_4 switches from southward between around 35.7 and 36.6 kg m^{-3} to northward between around 36.5 and 36.9 kg m^{-3} (Fig. 10c2). The double peak in the northward eddy-diffusive transport for PO_4 corresponds to locations of the local PO_4 extrema that characterize the UCDW and LCDW. We also note that, for all tracers, the profiles show a peak just below the base of the Ekman layer, indicating that the along-isopycnal tracer gradients are intense at that depth. The presence of this intense along-isopycnal tracer gradient suggests seasonal outcropping of the isopycnals ~ 36.3 to 36.6 kg m^{-3} south of the PF. Winter isopycnal outcropping leads to

ocean heat loss, O_2 ingassing, and CO_2 outgassing at the surface (not shown), as upwelled deep waters are relatively warm, rich in natural DIC, and poor in dissolved oxygen relative to the preindustrial atmosphere (e.g., Dong et al. 2007; Gruber et al. 2009; Garcia and Keeling 2001). Isopycnal outcropping also exposes waters to the euphotic zone, leading to DIC and PO_4 drawdown and O_2 production through photosynthesis. Along the seasonally outcropping isopycnals, we would thus expect a northward gradient of temperature, DIC, and PO_4 and a southward gradient of O_2 . These gradients would lead to a southward eddy-diffusive transport of temperature, DIC, and PO_4 and a northward diffusive transport of O_2 ; these features are visible in Figs. 10a–d2. Further support for this explanation comes from the distribution of an age tracer binned in (SSH; σ_2) space, which shows an intensified along-isopycnal gradient across the PF within this density range, indicating that these isopycnals are ventilated (i.e., in contact with the mixed layer over a seasonal cycle) south of the PF (not shown). Moreover, the seasonality of the eddy-diffusive transport reveals that the magnitude of the transport peaks in winter within this density range (not shown), supporting the idea of a winter outcropping of the isopycnals south of the PF which ventilates the ocean interior.

We now present a comparison of the magnitude of eddy-diffusive transport between the tracers in Fig. 10e. To do so, along-isopycnal tracer gradients are integrated along the PF and within its core layers and then divided by the corresponding time-mean component (blue bars in Figs. 8a2–a5). These gradients are scaled to an eddy-diffusive transport [χ_C ; Eq. (2)] using a κ of $500 \text{ m}^2 \text{ s}^{-1}$ that corresponds to the best agreement when estimating latitudinal profiles of χ_{temp} from Eq. (2) and from Lee et al.'s (2007) method. This value of κ lies at the low end of observational and theoretical values of 500 to $2000 \text{ m}^2 \text{ s}^{-1}$ for the Southern Ocean (e.g., Ferrari and Nikurashin 2010; Abernathey et al. 2010; LaCasce et al. 2014). We note that κ is expected to vary in space and time because of mean flow suppression (e.g., Ferrari and Nikurashin 2010). However, these variations are consistent across all tracers. By ignoring variations in κ , we are thus highlighting the dependence of eddy-diffusive transport on along-isopycnal tracer gradients and providing a comparison between different tracers. Across the PF core, the eddy-diffusive transport for temperature and O_2 is of the same order of magnitude as the corresponding time-mean component (Fig. 8a, blue bars), while eddy-diffusive transport for DIC and PO_4 is much weaker (less than 5% of the time mean). This difference in intensity is because isopycnal gradients of DIC and PO_4 are very weak, unlike those of

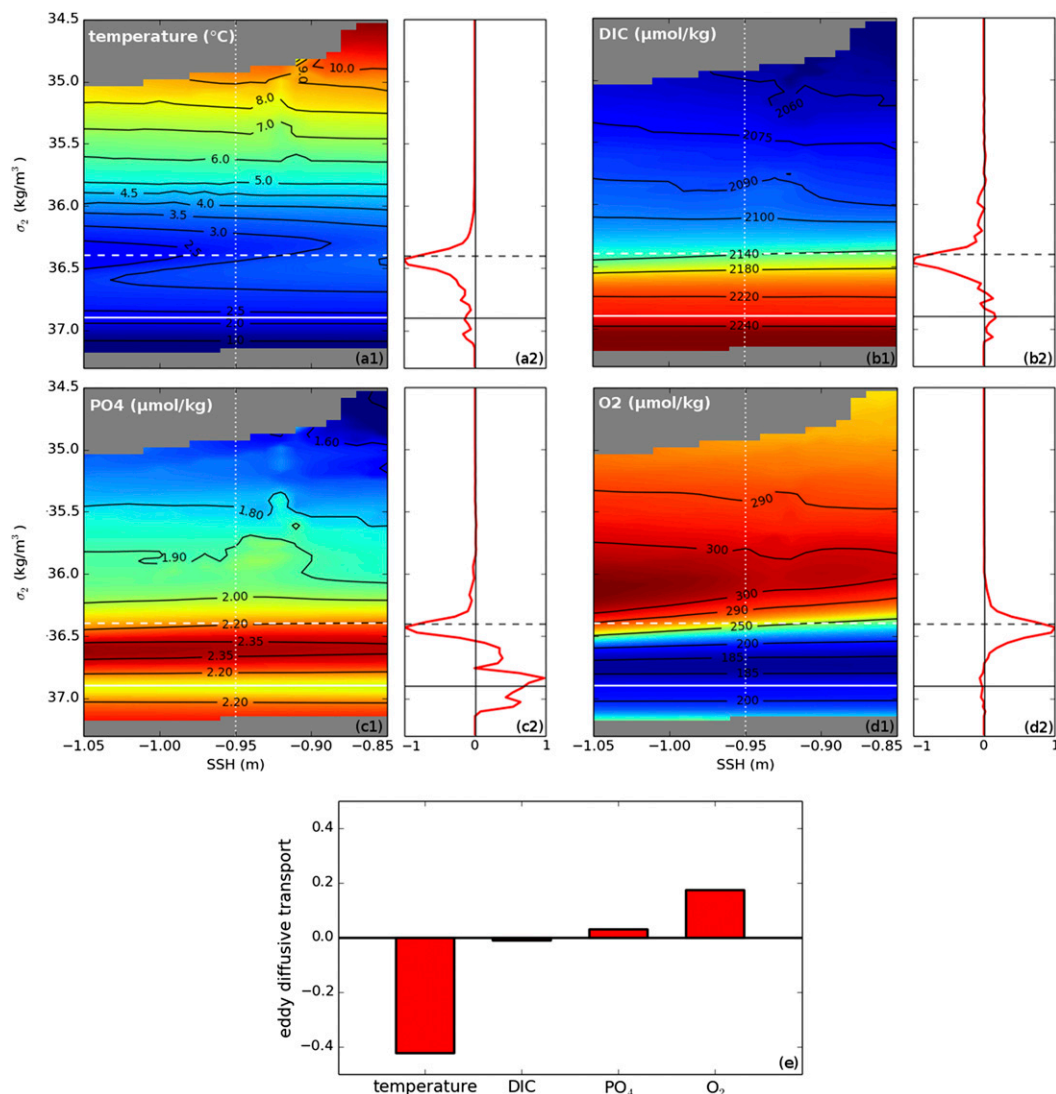


FIG. 10. 1) Tracers binned into SSH and σ_2 coordinates (colors) with solid black contours corresponding to the tracer isosurfaces. 2) Contribution of along-isopycnal tracer gradients to eddy-diffusive tracer transport across the PF [$-\oint \bar{h}(\nabla C) \cdot \mathbf{n} dl$; see Eq. (2)]. Vertical profiles have been normalized by their respective maximum absolute value. Positive values correspond to a northward eddy-diffusive transport. Dashed horizontal lines mark the base of the Ekman layer ($\sigma_2 = 36.4 \text{ kg m}^{-3}$) and solid horizontal lines the lower extension of the PF core ($\sigma_2 = 36.9 \text{ kg m}^{-3}$). Details of how the limits of the PF core and the Ekman layer are chosen are provided in section 2d. 1) White vertical dotted lines indicate the SSH contour corresponding to the position of the PF (-0.95 m). Results are presented for (a) temperature, (b) DIC, (c) PO₄, and (d) O₂. (e) Eddy-diffusive transport across the PF [Eq. (2)] summed over the PF core ($\sigma_2 \leq 36.9 \text{ kg m}^{-3}$) and normalized by the time-mean component (blue bars in Fig. 8a) for all four tracers.

temperature and O₂ (see Figs. 10a1–d1). To address potential ambiguity associated with the temperature scale, the diagnostic was also tested using temperature anomalies instead of absolute temperature. Using the time- and space-averaged temperature within the PF core, or the minimum temperature within the PF core, as a reference temperature does not affect the conclusion. Eddy-diffusive transport of temperature thus may

play an important role in the cross-frontal heat transport, reinforcing the eddy-advective component by fluxing heat southward, as demonstrated in previous studies (Gregory 2000; Lee et al. 2007; Morrison et al. 2013; Griffies et al. 2015). Eddy-diffusive transport of O₂ may also play an important role in the cross-frontal O₂ transport but opposes the eddy-advective component and thus reduces the total southward transport by

eddies. Conversely, both DIC and PO_4 eddy transports are dominated by the advective component with little contribution from eddy-diffusive transport. The differing contributions of eddy-diffusive components to the eddy transports of the four tracers play a role in the differing contributions of eddy transport to the total transport that we see in Fig. 8a. However, eddy-diffusive transports for biogeochemical tracers are small enough so that the ratio of the eddy to the time-mean components remain very similar to that of mass.

This qualitative assessment of the direction and intensity of tracer eddy-diffusive transport suggests that eddy-diffusive transport may provide a significant contribution to the southward eddy heat transport due to strong along-isopycnal temperature gradients.

4. Discussion

a. Relative contributions of eddy-advective and eddy-diffusive transports

The respective role and relative importance of the two processes by which mesoscale eddies transport tracers, namely, eddy-advective and eddy-diffusive transports, are topics of active debate. While estimating each component from observations remains a challenge (Palter et al. 2013), it has recently become possible in models with the advent of eddying climate models. Comparing the eddy-induced cross-frontal transports of heat, DIC, PO_4 , and O_2 and estimating their eddy-diffusive component, we find that eddy-advective transport is likely to be a leading-order component for all four tracers. Results for PO_4 are in line with the study of Lee and Williams (2000), which demonstrated that the advective component dominates over the diffusive component for long-lived nutrients. In the Southern Ocean, the biological pump has a relatively low efficiency due to limited availability of light and micronutrients, so that PO_4 can be considered a long-lived nutrient. Eddy-diffusive transport of heat is found to be important for eddy heat transport across the PF core, as isopycnal cross-frontal temperature gradients are strong over most layers of the PF core. Using 5-day-averaged output from a high-resolution model, Lee et al. (2007) computed meridional eddy-advective and eddy-diffusive transports for heat across constant latitudes of the Southern Ocean and found the latter to be around half the magnitude of the former, a result that is consistent with ours.

However, estimates of eddy-induced diffusive transport from Eq. (2) cannot provide accurate quantifications to conclude which of the two components of eddy heat transport is predominant or the importance of the eddy-diffusive component for the cross-frontal transport

of biogeochemical tracers. We identify here three main uncertainties in the estimate of eddy-diffusive transport: First, there is a broad range of values for the eddy-diffusivity coefficient κ that has been estimated from observations or calculated in models. Second, observations, theories, and models have all reported enhanced eddy diffusivities at the steering levels, that is, along the flanks of the jet and beneath its core (e.g., Abernathy et al. 2010; Ferrari and Nikurashin 2010; Naveira Garabato et al. 2011). In this study, we used a constant κ in space and time, which does not account for the typical enhanced values at the steering levels and at topographic obstacles. Third, while in the nearly adiabatic interior of the ocean, eddies stir tracers along isopycnals; in the surface diabatic ocean, they tend to stir tracers horizontally (Treguier et al. 1997; Ferrari et al. 2008). The surface diabatic layer mostly corresponds to the mixed layer, with an average depth around 100 m along the PF in the model and thus lies within the Ekman layer. In this study, we only investigated the tracer-diffusive transport from along-isopycnal tracer gradients, such that a part of the eddy-diffusive transport has been overlooked. Neglecting the horizontal eddy-diffusive transport might explain why the eddy-diffusive transport remains so low in layers lighter than 36.1 kg m^{-3} in our diagnostics (Figs. 10a2–d2). However, from the tracer distributions at the surface, we can infer that, in the mixed layer, eddies would diffuse heat southward, hence reinforcing the eddy heat advection, and diffuse biogeochemical tracers northward, hence opposing the eddy advection component. This inference still supports the results showing that eddy tracer advection is a leading-order component of the tracer transport across the PF core.

b. Comparison between the Polar Front and the Subantarctic Front

Another important front of the Southern Ocean is the SAF, which delimits the northern boundary of the ACC and sits between the subduction sites of AAIW and SAMW. This study presents results for the PF, the first front that upwelled heat, carbon, oxygen, and nutrients encounter on their route to lower latitudes. We also analyzed transport across the SAF and now summarize those results in comparison to the PF (Fig. 11).

Transport features across the PF discussed herein are also found to generally hold for the SAF, with an enhancement of tracer transport where the SAF encounters major topographic obstacles due both to an intensification of the eddy activity and misalignment of the mean flow with the path of the front. As for the PF, transport across the SAF core is largely dominated by the northward Ekman contribution. However, there is

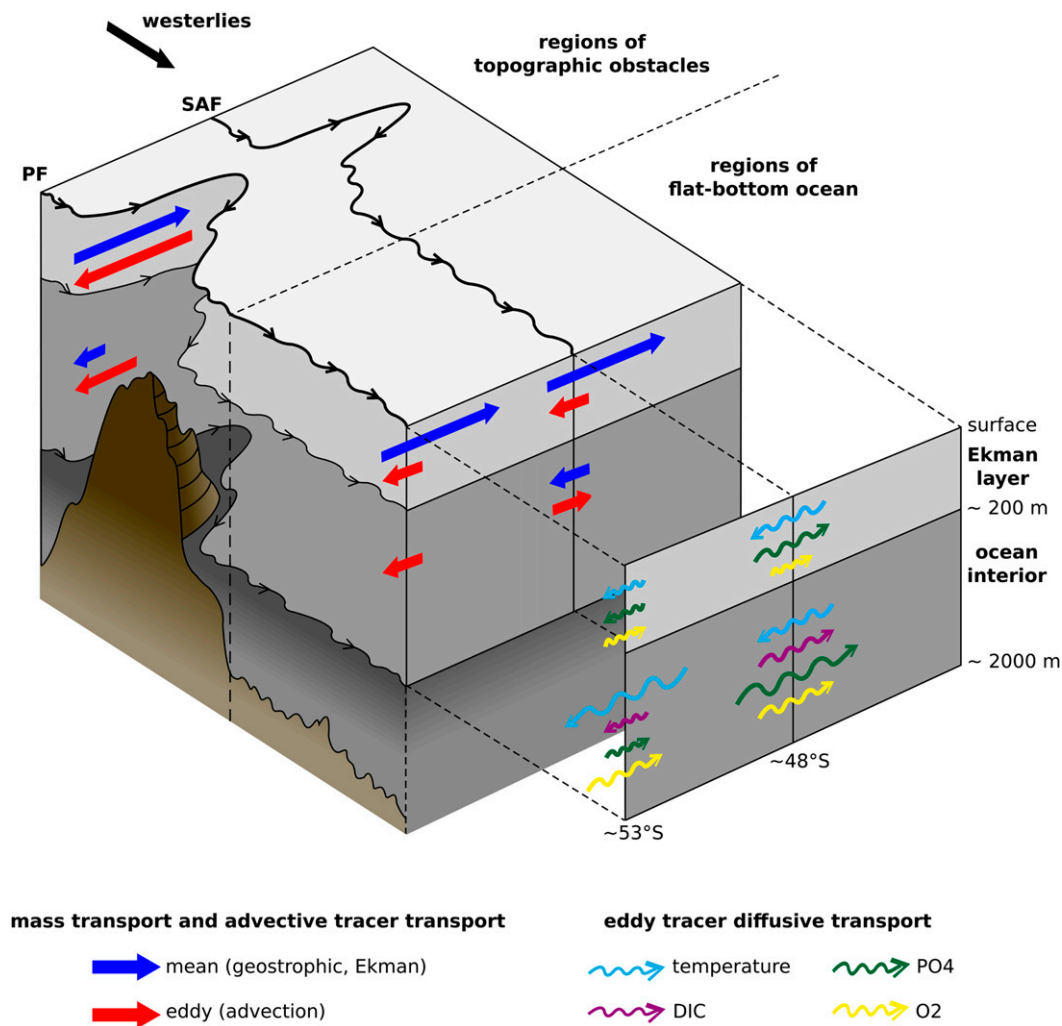


FIG. 11. Schematic of mass and tracer transport across the core of the PF and the SAF in regions of topographic obstacles and flat-bottom ocean. Our study considers ocean interior transport down to the bottom of the jet core (~ 2000 m). Straight arrows indicate the mass and advective tracer transports decomposed into time-mean component (blue) and eddy-advective component (red). Wavy arrows indicate the along-isopycnal eddy-diffusive transport for temperature (light blue), DIC (magenta), PO₄ (green), and O₂ (yellow). The size of the arrows scales qualitatively with the importance of the processes for total transport at each front, with a missing arrow meaning that the process was found to have a negligible contribution to the total transport. Note that wavy arrows (i) are not on the same scale as straight arrows, as time-mean transport is found to be generally much stronger than eddy-diffusive transport for tracers (see section 3b), and (ii) show the alongfront-averaged eddy-diffusive transport for tracers, as differences between eddy tracer-diffusive transport in regions of topographic obstacles and flat-bottom ocean have not been investigated in this study.

no eddy-prevailing regime below the Ekman layer but rather a combined contribution from eddies and geostrophic time-mean transport. As a result, the eddy effect on the total tracer transport across the SAF is weaker than across the PF, and a larger part of the southward transport is supported by geostrophic time-mean transport including near-topographic obstacles.

Eddy-advective transport dominates eddy tracer transport across the SAF core with two notable exceptions (Fig. 11). Eddy-diffusive transport for PO₄

contributes a significant northward transport across the SAF that generally reinforces eddy-advective transport below the Ekman layer. As a result, PO₄ is the only tracer showing a net northward eddy transport across the SAF core. Eddy-diffusive transport for heat may dominate over the advective component below the Ekman layer, hence strongly reinforcing the southward geostrophic transport across the SAF core. However, eddy-diffusive transport for heat is generally weaker across the SAF than across the PF,

as isotherms tend to be more aligned with isopycnals at lower latitudes. The SAF is indeed known to mark a transition in the balance of stratification in the Southern Ocean from temperature and salinity equally contributing to stratification south of the SAF to a temperature-dominated stratification north of the SAF (Pollard et al. 2002). Overall, the role of eddy-diffusive transport for biogeochemical tracers is more important across the SAF core than across the PF core, due both to the role of eddy-advective transport being weaker and isopycnal tracer gradients being stronger at the SAF (in particular for DIC and PO_4).

5. Summary

This study uses an eddy-rich climate model coupled to a simplified biogeochemical model to examine the processes driving the transport of heat, carbon, oxygen, and nutrients (phosphate) across the Polar Front (PF) and above the sill of major topographic obstacles, a region referred to as the PF core. We focus on the role of mesoscale eddies relative to other processes, in particular the Ekman transport whose role has received much attention so far. We find the following:

- Mesoscale eddies transport tracers southward across the PF core. In the Ekman layer, southward eddy transport partially compensates the intense northward Ekman transport, which is the main driver of tracer transport across the PF core. Below the Ekman layer, southward eddy transport dominates the total transport, hence supporting the transport of tracers to the Antarctic Divergence. However, most of the southward branch of the upper cell of the meridional overturning is found to be achieved by geostrophic currents that lie below the PF core.
- Eddy transport is mostly localized at and near major topographic obstacles. At major topographic obstacles, eddies dominate the total transport across the PF core. Hence, hotspots are found to be privileged pathways for water and tracers toward high latitudes.
- Eddy-advective transport is the leading-order component of eddy transport for heat and biogeochemical tracers across the PF core. Eddy-diffusive transport may significantly reinforce eddy-advective transport for heat because of intense northward along-isopycnal temperature gradients across the PF core. In contrast, eddy-diffusive transport for biogeochemical tracers is either small, because of weak along-isopycnal biogeochemical tracer gradients, or opposes the eddy-advective component.

Acknowledgments. The CM2.6–miniBLING control simulation was run at GFDL through a large cooperative effort involving a substantial commitment of computational resources and data storage. C. O. Dufour was supported by the National Aeronautics and Space Administration (NASA) under Award NNX14AL40G and by the Princeton Environmental Institute Grand Challenge initiative. G. F. de Souza was supported by the Swiss National Science Foundation (SNSF) Postdoctoral Fellowship P300P2-147747 and NASA under Award NNX14AL40G. A. K. Morrison was supported by the U.S. Department of Energy under Award DE-SC0012457. I. Frenger was supported by the SNSF Early Postdoc Mobility Fellowship P2EZP2-152133. J. L. Sarmiento was supported by the Southern Ocean Carbon and Climate Observations and Modeling (SOCCOM) project under the National Science Foundation Award PLR-1425989. R. D. Slater was supported by NASA under Award NNX14AL40G. We thank Michael Winton, Alison Gray, and Robert Hallberg for helpful comments and discussions on this manuscript and Youngrak Cho for his technical help on the schematic of Fig. 11. We are very grateful to Andrew Thompson for providing sound and insightful comments through several rounds of reviews that greatly improved this manuscript. We also thank an anonymous reviewer for useful comments.

APPENDIX A

Computation of Cross-Frontal Mass and Tracer Transport

a. Kinematics of cross-frontal transport

Let us define a generalized meridional coordinate:

$$s(x, y, t) = y - \phi(x, t), \quad (\text{A1})$$

where $\phi(x, t)$ measures the meridional position of the front (i.e., a SSH contour that we assume monotonic with latitude) as a function of zonal position and time. The volume transport crossing the front is proportional to the diasurface velocity component [e.g., see section 6.7 of Griffies (2004)], which is given by

$$\mathcal{V} = \frac{ds}{dt} = \frac{d(y - \phi)}{dt} = v - (\partial_t + u\partial_x)\phi, \quad (\text{A2})$$

The diasurface velocity is composed of three contributions: the meridional velocity component v , the local time tendency of the contour $\partial_t\phi$, and the zonal advection of the contour $u\partial_x\phi$. Taking the climatological monthly mean yields

$$\overline{\mathcal{V}} = \overline{v} - \overline{\partial_t \phi} - \overline{u \partial_x \phi} = \overline{v} - \overline{\partial_t \phi} - \overline{u \partial_x \phi} - \overline{u' \partial_x \phi'}, \quad (\text{A3})$$

where the overbar is a time mean and primes are deviations from the mean. Our study considers the flux across a monthly climatology of the front. Hence, we compute the flux while following the monthly climatological fluctuations of the front position and thus ignoring the flux across higher time frequency fluctuations. Hence, the second and fourth terms of the right-hand side of Eq. (A3) drop. We acknowledge that those terms can lead to significant fluxes as the front position and the velocities at that position fluctuate instantaneously. These components are, however, not represented in our analysis, whereby we diagnose

$$\overline{\mathcal{V}} = \overline{v} - \overline{u \partial_x \phi}. \quad (\text{A4})$$

Similar arguments lead to the climatological mean tracer flux across the front:

$$\overline{C\mathcal{V}} = \overline{C}\overline{\mathcal{V}} + \overline{C'(v' - u' \partial_x \phi)}. \quad (\text{A5})$$

b. Computation in the model

To compute the tracer transport Φ across the front in the model, meridional and zonal advective fluxes of the tracer are integrated along the discretized front path. For a given month,

$$d\Phi = \rho_0 C \mathcal{V} dS, \quad (\text{A6})$$

where ρ_0 is the constant Boussinesq reference density set to 1035 kg m^{-3} ; C is the tracer concentration; \mathcal{V} is the diasurface velocity described earlier; and dS is the discretized surface area at the frontal section that has the dimension of the frontal segment times depth (i.e., $dx dz$ or $dy dz$). Hence, transports look different from fluxes because dS varies in space. The concentration C is taken equal to unity to compute mass transport across the front. As mass transport is nonzero across the core of the front, we calculate temperature transport (with temperature in $^{\circ}\text{C}$) and express this transport as heat transport equivalent in watts using an ocean heat capacity of $3992.1 \text{ J kg}^{-1} \text{ K}^{-1}$. The velocity \mathcal{V} is composed of the velocity resolved by the model so that the parameterized submesoscale eddy-induced velocity is ignored here. The transport $d\Phi$ can have both a zonal and a meridional component depending on the orientation of the front, with $d\Phi > 0$ indicating northward transport if the front path follows a constant latitude. For the sake of simplicity, we use northward for positive transports and southward for negative transports, bearing in mind that the zonal component of the cross-frontal

transport is likely to play an important role, particularly in regions where the front meanders. We applied Eq. (A6) to determine mass and tracer transports across the PF at every vertical level and bin of longitude in the model (i.e., at every 0.1° , which is the horizontal grid resolution).

APPENDIX B

Binning Procedure

Variables on the model's native z^* coordinate are binned into 100 fixed but unevenly spaced σ_2 classes whose spacing decreases with depth. We use a binning procedure similar to the one described in Lee et al. (2007) where properties and transports are conserved. A 20-yr monthly climatology of σ_2 is used to bin Φ_{mean} , while monthly mean σ_2 are used to bin Φ_{total} [Eq. (1)]. There is thus an error associated with using monthly mean σ_2 (offline binning) instead of every time-step σ_2 (online binning) for the total component. However, this error was evaluated by comparing an online and offline binning of the meridional total transport for mass and found to be small enough [$O(10\%)$] so that the conclusions presented here are not affected.

REFERENCES

- Abernathey, R., and P. Cessi, 2014: Topographic enhancement of eddy efficiency in baroclinic equilibration. *J. Phys. Oceanogr.*, **44**, 2107–2126, doi:10.1175/JPO-D-14-0014.1.
- , J. Marshall, M. Mazloff, and E. Shuckburgh, 2010: Enhancement of mesoscale eddy stirring at steering levels in the Southern Ocean. *J. Phys. Oceanogr.*, **40**, 170–184, doi:10.1175/2009JPO4201.1.
- Anson, I., J. Jackson, K. Reid, J. Durgadoo, S. Swart, and S. Eberenz, 2014: Evidence of a southward eddy corridor in the south-west Indian Ocean. *Deep-Sea Res. II*, **119**, 69–76, doi:10.1016/j.dsr2.2014.05.012.
- Ballarotta, M., S. Drijfhout, T. Kuhlbrodt, and K. Döös, 2013: The residual circulation of the Southern Ocean: Which spatio-temporal scales are needed? *Ocean Modell.*, **64**, 46–55, doi:10.1016/j.oceanmod.2013.01.005.
- Belkin, I. M., and A. L. Gordon, 1996: Southern Ocean fronts from the Greenwich meridian to Tasmania. *J. Geophys. Res.*, **101**, 3675–3696, doi:10.1029/95JC02750.
- Bishop, S. P., 2013: Divergent eddy heat fluxes in the Kuroshio Extension at 144° – 148°E . Part II: Spatiotemporal variability. *J. Phys. Oceanogr.*, **43**, 2416–2431, doi:10.1175/JPO-D-13-061.1.
- Bower, A. S., H. T. Rossby, and J. L. Lillibridge, 1985: The Gulf Stream—Barrier or blender? *J. Phys. Oceanogr.*, **15**, 24–32, doi:10.1175/1520-0485(1985)015<0024:TGSOB>2.0.CO;2.
- Bryan, F. O., P. R. Gent, and R. Tomas, 2014: Can Southern Ocean eddy effects be parameterized in climate models? *J. Climate*, **27**, 411–425, doi:10.1175/JCLI-D-12-00759.1.
- Chapman, C. C., 2014: Southern Ocean jets and how to find them: Improving and comparing common jet detection methods.

- J. Geophys. Res. Oceans*, **119**, 4318–4339, doi:10.1002/2014JC009810.
- Cheon, W. G., Y.-G. Park, J. R. Toggweiler, and S.-K. Lee, 2014: The relationship of Weddell Polynya and open-ocean deep convection to the Southern Hemisphere westerlies. *J. Phys. Oceanogr.*, **44**, 694–713, doi:10.1175/JPO-D-13-0112.1.
- Chidichimo, M. P., K. A. Donohue, D. R. Watts, and K. L. Tracey, 2014: Baroclinic transport time series of the Antarctic Circumpolar Current measured in Drake Passage. *J. Phys. Oceanogr.*, **44**, 1829–1853, doi:10.1175/JPO-D-13-071.1.
- Cunningham, S. A., S. G. Alderson, B. A. King, and M. A. Brandon, 2003: Transport and variability of the Antarctic Circumpolar Current in Drake Passage. *J. Geophys. Res.*, **108**, 8084, doi:10.1029/2001JC001147.
- Delworth, T. L., and Coauthors, 2012: Simulated climate and climate change in the GFDL CM2.5 High-Resolution Coupled Climate Model. *J. Climate*, **25**, 2755–2781, doi:10.1175/JCLI-D-11-00316.1.
- de Szoek, R. A., and M. D. Levine, 1981: The advective flux of heat by mean geostrophic motions in the Southern Ocean. *Deep-Sea Res.*, **28A**, 1057–1085, doi:10.1016/0198-0149(81)90048-0.
- DeVries, T., and F. Primeau, 2011: Dynamically and observationally constrained estimates of water-mass distributions and ages in the global ocean. *J. Phys. Oceanogr.*, **41**, 2381–2401, doi:10.1175/JPO-D-10-05011.1.
- Dong, S., S. T. Gille, and J. Sprintall, 2007: An assessment of the Southern Ocean mixed layer heat budget. *J. Climate*, **20**, 4425–4442, doi:10.1175/JCLI4259.1.
- Downes, S. M., A. Gnanadesikan, S. M. Griffies, and J. L. Sarmiento, 2011: Water mass exchange in the Southern Ocean in coupled climate models. *J. Phys. Oceanogr.*, **41**, 1756–1771, doi:10.1175/2011JPO4586.1.
- Dufour, C. O., J. Le Sommer, T. Penduff, B. Barnier, and M. H. England, 2011: Structure and causes of the pulsation mode in the Antarctic Circumpolar Current south of Australia. *J. Phys. Oceanogr.*, **41**, 253–268, doi:10.1175/2010JPO4193.1.
- , —, J. D. Zika, M. Gehlen, J. C. Orr, P. Mathiot, and B. Barnier, 2012: Standing and transient eddies in the response of the Southern Ocean meridional overturning to the southern annular mode. *J. Climate*, **25**, 6958–6974, doi:10.1175/JCLI-D-11-00309.1.
- , —, M. Gehlen, J. C. Orr, J.-M. Molines, J. Simeon, and B. Barnier, 2013: Eddy compensation and controls of the enhanced sea-to-air CO₂ flux during positive phases of the southern annular mode. *Global Biogeochem. Cycles*, **27**, 950–961, doi:10.1002/gbc.20090.
- Ferrari, R., and M. Nikurashin, 2010: Suppression of eddy diffusivity across jets in the Southern Ocean. *J. Phys. Oceanogr.*, **40**, 1501–1519, doi:10.1175/2010JPO4278.1.
- , J. C. McWilliams, V. M. Canuto, and M. Dubovikov, 2008: Parameterization of eddy fluxes near oceanic boundaries. *J. Climate*, **21**, 2770–2789, doi:10.1175/2007JCLI1510.1.
- Fox-Kemper, B., R. Ferrari, and J. Pedlosky, 2003: On the indeterminacy of rotational and divergent eddy fluxes. *J. Phys. Oceanogr.*, **33**, 478–483, doi:10.1175/1520-0485(2003)033<0478:OTIORA>2.0.CO;2.
- , and Coauthors, 2011: Parameterization of mixed layer eddies. III: Implementation and impact in global ocean climate simulations. *Ocean Modell.*, **39**, 61–78, doi:10.1016/j.ocemod.2010.09.002.
- Galbraith, E. D., A. Gnanadesikan, J. P. Dunne, and M. R. Hiscock, 2010: Regional impacts of iron-light colimitation in a global biogeochemical model. *Biogeosciences*, **7**, 1043–1064, doi:10.5194/bg-7-1043-2010.
- Garcia, H. E., and R. F. Keeling, 2001: On the global oxygen anomaly and air-sea flux. *J. Geophys. Res.*, **106**, 31 155–31 166, doi:10.1029/1999JC000200.
- , R. A. Locarnini, T. P. Boyer, J. I. Antonov, O. K. Baranova, M. M. Zweng, and D. R. Johnson, 2010a: *Dissolved Oxygen, Apparent Oxygen Utilization, and Oxygen Saturation*. Vol. 3, *World Ocean Atlas 2009*, NOAA Atlas NESDIS 70, 344 pp.
- , —, —, —, —, —, and —, 2010b: *Nutrients (Phosphate, Nitrate, Silicate)*, Vol. 4, *World Ocean Atlas 2009*, NOAA Atlas NESDIS 71, 398 pp.
- Gent, P. R., and J. C. McWilliams, 1990: Isopycnal mixing in ocean circulation models. *J. Phys. Oceanogr.*, **20**, 150–155, doi:10.1175/1520-0485(1990)020<0150:IMIOCM>2.0.CO;2.
- , J. Willebrand, T. J. McDougall, and J. C. McWilliams, 1995: Parameterizing eddy-induced tracer transports in ocean circulation models. *J. Phys. Oceanogr.*, **25**, 463–474, doi:10.1175/1520-0485(1995)025<0463:PEITTI>2.0.CO;2.
- Gille, S. T., 1994: Mean sea surface height of the Antarctic Circumpolar Current from Geosat data: Method and application. *J. Geophys. Res.*, **99**, 18 255–18 273, doi:10.1029/94JC01172.
- Gouretski, V. V., and A. I. Danilov, 1994: Characteristics of warm rings in the African sector of the Antarctic Circumpolar Current. *Deep-Sea Res. I*, **41**, 1131–1157, doi:10.1016/0967-0637(94)90037-X.
- Graham, R. M., A. M. de Boer, K. J. Heywood, M. R. Chapman, and D. P. Stevens, 2012: Southern Ocean fronts: Controlled by wind or topography? *J. Geophys. Res.*, **117**, C08018, doi:10.1029/2012JC007887.
- Gregory, J. M., 2000: Vertical heat transports in the ocean and their effect on time-dependent climate change. *Climate Dyn.*, **16**, 501–515, doi:10.1007/s003820000059.
- Griessel, A., S. T. Gille, J. Sprintall, J. L. McClean, and M. E. Maltrud, 2009: Assessing eddy heat flux and its parameterization: A wavenumber perspective from a 1/10° ocean simulation. *Ocean Modell.*, **29**, 248–260, doi:10.1016/j.ocemod.2009.05.004.
- Griffies, S., 2004: *Fundamentals of Ocean Climate Models*. Princeton University Press, 518 pp.
- , 2012: Elements of the Modular Ocean Model (MOM). NOAA GFDL Ocean Group Tech. Rep. 7, 618 pp. [Available online at http://www.mom-ocean.org/web/docs/project/MOM5_elements.pdf.]
- , and Coauthors, 2015: Impacts on ocean heat from transient mesoscale eddies in a hierarchy of climate models. *J. Climate*, **28**, 952–977, doi:10.1175/JCLI-D-14-00353.1.
- Gruber, N., and Coauthors, 2009: Oceanic sources, sinks, and transport of atmospheric CO₂. *Global Biogeochem. Cycles*, **23**, GB1005, doi:10.1029/2008GB003349.
- Hallberg, R., 2013: Using a resolution function to regulate parameterizations of oceanic mesoscale eddy effects. *Ocean Modell.*, **72**, 92–103, doi:10.1016/j.ocemod.2013.08.007.
- , and A. Gnanadesikan, 2006: The role of eddies in determining the structure and response of the wind-driven Southern Hemisphere overturning: Results from the Modeling Eddies in the Southern Ocean (MESO) project. *J. Phys. Oceanogr.*, **36**, 2232–2252, doi:10.1175/JPO2980.1.
- Hirabara, M., H. Tsujino, H. Nakano, and G. Yamanaka, 2012: Formation mechanism of the Weddell Sea polynya and the impact on the global abyssal ocean. *J. Oceanogr.*, **68**, 771–796, doi:10.1007/s10872-012-0139-3.
- Holte, J. W., L. D. Talley, T. K. Chereskin, and B. M. Sloyan, 2013: Subantarctic mode water in the southeast Pacific: Effect of

- exchange across the Subantarctic Front. *J. Geophys. Res. Oceans*, **118**, 2052–2066, doi:10.1002/jgrc.20144.
- Ito, T., M. Woloszyn, and M. Mazloff, 2010: Anthropogenic carbon dioxide transport in the Southern Ocean driven by Ekman flow. *Nature*, **463**, 80–83, doi:10.1038/nature08687.
- Key, R. M., and Coauthors, 2004: A global ocean carbon climatology: Results from Global Data Analysis Project (GLODAP). *Global Biogeochem. Cycles*, **18**, GB4031, doi:10.1029/2004GB002247.
- Khatiwala, S., F. Primeau, and M. Holzer, 2012: Ventilation of the deep ocean constrained with tracer observations and implications for radiocarbon estimates of ideal mean age. *Earth Planet. Sci. Lett.*, **325–326**, 116–125, doi:10.1016/j.epsl.2012.01.038.
- Kwon, E. Y., S. M. Downes, J. L. Sarmiento, R. Farneti, and C. Deutsch, 2013: Role of the seasonal cycle in the subduction rates of upper Southern Ocean waters. *J. Phys. Oceanogr.*, **43**, 1096–1113, doi:10.1175/JPO-D-12-060.1.
- LaCasce, J. H., R. Ferrari, J. Marshall, R. Tulloch, D. Balwada, and K. Speer, 2014: Float-derived isopycnal diffusivities in the DIMES experiment. *J. Phys. Oceanogr.*, **44**, 764–780, doi:10.1175/JPO-D-13-0175.1.
- Langlais, C., S. Rintoul, and A. Schiller, 2011: Variability and mesoscale activity of the Southern Ocean fronts: Identification of a circumpolar coordinate system. *Ocean Modell.*, **39**, 79–96, doi:10.1016/j.ocemod.2011.04.010.
- Lee, M.-M., and R. G. Williams, 2000: The role of eddies in the isopycnal transfer of nutrients and their impact on biological production. *J. Mar. Res.*, **58**, 895–917, doi:10.1357/002224000763485746.
- , D. P. Marshall, and R. G. Williams, 1997: On the eddy transfer of tracers: Advective or diffusive? *J. Mar. Res.*, **55**, 483–505, doi:10.1357/0022240973224346.
- , A. J. G. Nurser, A. C. Coward, and B. A. de Cuevas, 2007: Eddy advective and diffusive transports of heat and salt in the Southern Ocean. *J. Phys. Oceanogr.*, **37**, 1376–1393, doi:10.1175/JPO3057.1.
- Legg, S., R. W. Hallberg, and J. B. Girton, 2006: Comparison of entrainment in overflows simulated by z -coordinate, isopycnal and non-hydrostatic models. *Ocean Modell.*, **11**, 69–97, doi:10.1016/j.ocemod.2004.11.006.
- Locarnini, R. A., A. V. Mishonov, J. I. Antonov, T. P. Boyer, H. E. Garcia, O. K. Baranova, M. M. Zweng, and D. R. Johnson, 2010: *Temperature*. Vol. 1, *World Ocean Atlas 2009*, NOAA Atlas NESDIS 68, 184 pp.
- Lozier, M. S., L. J. Pratt, A. M. Rogerson, and P. D. Miller, 1997: Exchange geometry revealed by float trajectories in the Gulf Stream. *J. Phys. Oceanogr.*, **27**, 2327–2341, doi:10.1175/1520-0485(1997)027<2327:EGRBFT>2.0.CO;2.
- Lumpkin, R., and K. Speer, 2007: Global ocean meridional overturning. *J. Phys. Oceanogr.*, **37**, 2550–2562, doi:10.1175/JPO3130.1.
- Marshall, J., and G. Shutts, 1981: A note on rotational and divergent eddy fluxes. *J. Phys. Oceanogr.*, **11**, 1677–1680, doi:10.1175/1520-0485(1981)011<1677:ANORAD>2.0.CO;2.
- , and K. Speer, 2012: Closure of the meridional overturning circulation through Southern Ocean upwelling. *Nat. Geosci.*, **5**, 171–180, doi:10.1038/ngeo1391.
- Mazloff, M. R., R. Ferrari, and T. Schneider, 2013: The force balance of the Southern Ocean meridional overturning circulation. *J. Phys. Oceanogr.*, **43**, 1193–1208, doi:10.1175/JPO-D-12-069.1.
- Meredith, M. P., and A. M. Hogg, 2006: Circumpolar response of Southern Ocean eddy activity to a change in the southern annular mode. *Geophys. Res. Lett.*, **33**, L16608, doi:10.1029/2006GL026499.
- Morrison, A. K., O. A. Saenko, A. M. Hogg, and P. Spence, 2013: The role of vertical eddy flux in Southern Ocean heat uptake. *Geophys. Res. Lett.*, **40**, 5445–5450, doi:10.1002/2013GL057706.
- , T. L. Frölicher, and J. L. Sarmiento, 2015: Upwelling in the Southern Ocean. *Phys. Today*, **68**, 27–32, doi:10.1063/PT.3.2654.
- Morrow, R., M. L. Ward, A. M. Hogg, and S. Pasquet, 2010: Eddy response to Southern Ocean climate modes. *J. Geophys. Res.*, **115**, C10030, doi:10.1029/2009JC005894.
- Naveira Garabato, A. C., R. Ferrari, and K. L. Polzin, 2011: Eddy stirring in the Southern Ocean. *J. Geophys. Res.*, **116**, C09019, doi:10.1029/2010JC006818.
- Olbers, D., D. Borowski, C. Völker, and J.-O. Wolff, 2004: The dynamical balance, transport and circulation of the Antarctic Circumpolar Current. *Antarct. Sci.*, **16**, 439–470, doi:10.1017/S0954102004002251.
- Orsi, A. H., and T. Whitworth III, 2005: *Southern Ocean*. Vol. 1, *Hydrographic Atlas of the World Ocean Circulation Experiment (WOCE)*. M. Sparrow, P. Chapman, and J. Gould, Ed., International WOCE Project Office, 223 pp.
- , —, and W. D. Nowlin Jr., 1995: On the meridional extent and fronts of the Antarctic Circumpolar Current. *Deep-Sea Res. I*, **42**, 641–673, doi:10.1016/0967-0637(95)00021-W.
- Palter, J. B., J. L. Sarmiento, A. Gnanadesikan, J. Simeon, and R. D. Slater, 2010: Fueling export production: Nutrient return pathways from the deep ocean and their dependence on the meridional overturning circulation. *Biogeosciences*, **7**, 3549–3568, doi:10.5194/bg-7-3549-2010.
- , I. Marinov, J. L. Sarmiento, and N. Gruber, 2013: Large-scale, persistent nutrient fronts of the world ocean: Impacts on biogeochemistry. *Chemical Oceanography of Frontal Zones*, I. M. Belkin, Ed., Springer-Verlag, 1–38, doi:10.1007/978_2013_241.
- Peña Molino, B., S. R. Rintoul, and M. R. Mazloff, 2014: Barotropic and baroclinic contributions to along-stream and across-stream transport in the Antarctic Circumpolar Current. *J. Geophys. Res. Oceans*, **119**, 8011–8028, doi:10.1002/2014JC010020.
- Phillips, H. E., and N. L. Bindoff, 2014: On the nonequivalent barotropic structure of the Antarctic Circumpolar Current: An observational perspective. *J. Geophys. Res. Oceans*, **119**, 5221–5243, doi:10.1002/2013JC009516.
- Pollard, R., M. Lucas, and J. Read, 2002: Physical controls on biogeochemical zonation in the Southern Ocean. *Deep-Sea Res. II*, **49**, 3289–3305, doi:10.1016/S0967-0645(02)00084-X.
- Redi, M. H., 1982: Oceanic isopycnal mixing by coordinate rotation. *J. Phys. Oceanogr.*, **12**, 1154–1158, doi:10.1175/1520-0485(1982)012<1154:OIMBCR>2.0.CO;2.
- Rintoul, S. R., and M. H. England, 2002: Ekman transport dominates local air–sea fluxes in driving variability of Subantarctic Mode Water. *J. Phys. Oceanogr.*, **32**, 1308–1321, doi:10.1175/1520-0485(2002)032<1308:ETDLAS>2.0.CO;2.
- Roberts, M. J., and D. P. Marshall, 2000: On the validity of downgradient eddy closures in ocean models. *J. Geophys. Res. Oceans*, **105**, 28 613–28 627, doi:10.1029/1999JC000041.
- Sallée, J. B., K. Speer, and R. Morrow, 2008a: Response of the Antarctic Circumpolar Current to atmospheric variability. *J. Climate*, **21**, 3020–3039, doi:10.1175/2007JCLI1702.1.
- , —, —, and R. Lumpkin, 2008b: An estimate of Lagrangian eddy statistics and diffusion in the mixed layer of the Southern Ocean. *J. Mar. Res.*, **66**, 441–463, doi:10.1357/002224008787157458.
- , E. Shuckburgh, N. Bruneau, A. J. S. Meijers, T. J. Bracegirdle, Z. Wang, and T. Roy, 2013: Assessment of Southern Ocean

- water mass circulation and characteristics in CMIP5 models: Historical bias and forcing response. *J. Geophys. Res. Oceans*, **118**, 1830–1844, doi:10.1002/jgrc.20135.
- Samelson, R. M., 1992: Fluid exchange across a meandering jet. *J. Phys. Oceanogr.*, **22**, 431–444, doi:10.1175/1520-0485(1992)022<0431:FEAAMJ>2.0.CO;2.
- Sarmiento, J. L., N. Gruber, M. A. Brzezinski, and J. P. Dunne, 2004: High-latitude controls of thermocline nutrients and low latitude biological productivity. *Nature*, **427**, 56–60, doi:10.1038/nature02127.
- Shakespeare, C. J., and A. M. Hogg, 2012: An analytical model of the response of the meridional overturning circulation to changes in wind and buoyancy forcing. *J. Phys. Oceanogr.*, **42**, 1270–1287, doi:10.1175/JPO-D-11-0198.1.
- Smith, K. S., and J. Marshall, 2009: Evidence for enhanced eddy mixing at middepth in the Southern Ocean. *J. Phys. Oceanogr.*, **39**, 50–69, doi:10.1175/2008JPO3880.1.
- Sokolov, S., and S. R. Rintoul, 2007: Multiple jets of the Antarctic Circumpolar Current south of Australia. *J. Phys. Oceanogr.*, **37**, 1394–1412, doi:10.1175/JPO3111.1.
- Solomon, H., 1971: On the representation of isentropic mixing in ocean circulation models. *J. Phys. Oceanogr.*, **1**, 233–234, doi:10.1175/1520-0485(1971)001<0233:OTROIM>2.0.CO;2.
- Sommeria, J., S. D. Meyers, and H. L. Swinney, 1989: Laboratory model of a planetary eastward jet. *Nature*, **337**, 58–61, doi:10.1038/337058a0.
- Spence, P., E. van Sebille, O. A. Saenko, and M. H. England, 2014: Using Eulerian and Lagrangian approaches to investigate wind-driven changes in the Southern Ocean abyssal circulation. *J. Phys. Oceanogr.*, **44**, 662–675, doi:10.1175/JPO-D-13-0108.1.
- Talley, L. D., 2013: Closure of the global overturning circulation through the Indian, Pacific, and Southern Oceans: Schematics and transports. *Oceanography*, **26**, 80–97, doi:10.5670/oceanog.2013.07.
- Thompson, A. F., and J.-B. Sallée, 2012: Jets and topography: Jet transitions and the impact on transport in the Antarctic Circumpolar Current. *J. Phys. Oceanogr.*, **42**, 956–972, doi:10.1175/JPO-D-11-0135.1.
- Treguier, A. M., I. M. Held, and V. D. Larichev, 1997: Parameterization of quasigeostrophic eddies in primitive equation ocean models. *J. Phys. Oceanogr.*, **27**, 567–580, doi:10.1175/1520-0485(1997)027<0567:POQEIP>2.0.CO;2.
- , M. H. England, S. R. Rintoul, G. Madec, J. Le Sommer, and J.-M. Molines, 2007: Southern Ocean overturning across streamlines in an eddying simulation of the Antarctic Circumpolar Current. *Ocean Sci.*, **3**, 491–507, doi:10.5194/os-3-491-2007.
- Whitworth, T., 1983: Monitoring the transport of the Antarctic Circumpolar Current at Drake Passage. *J. Phys. Oceanogr.*, **13**, 2045–2057, doi:10.1175/1520-0485(1983)013<2045:MTTOTA>2.0.CO;2.
- , and R. G. Peterson, 1985: Volume transport of the Antarctic Circumpolar Current from bottom pressure measurements. *J. Phys. Oceanogr.*, **15**, 810–816, doi:10.1175/1520-0485(1985)015<0810:VTOTAC>2.0.CO;2.
- Wiggins, S., 2005: The dynamical systems approach to Lagrangian transport in oceanic flows. *Annu. Rev. Fluid Mech.*, **37**, 295–328, doi:10.1146/annurev.fluid.37.061903.175815.
- Winton, M., R. Hallberg, and A. Gnanadesikan, 1998: Simulation of density-driven frictional downslope flow in z -coordinate ocean models. *J. Phys. Oceanogr.*, **28**, 2163–2174, doi:10.1175/1520-0485(1998)028<2163:SODDFD>2.0.CO;2.
- Zika, J. D., and Coauthors, 2013: Vertical eddy fluxes in the Southern Ocean. *J. Phys. Oceanogr.*, **43**, 941–955, doi:10.1175/JPO-D-12-0178.1.